SUPERVISED BINARY HYPERBOLIC EMBEDDINGS

Anonymous authors
Paper under double-blind review

ABSTRACT

As datasets grow in size, vector-based search becomes increasingly challenging in terms of both storage and computational efficiency. Traditional solutions such as quantization techniques involve trade-offs between retrieval speed and accuracy, while hashing methods often require further optimization for binarization. In this work, we propose leveraging the compact nature of hyperbolic space for efficient search. Specifically, we introduce Binary Hyperbolic Embeddings, which transform complex hyperbolic similarity calculations into binary operations. We prove that these binary hyperbolic embeddings are retrieval equivalent to their real-valued counterparts, ensuring minimal loss in retrieval quality. Our approach can be seamlessly integrated into FAISS to obtain real-world improved memory efficiency and running speed while maintaining performance comparable to full-precision Euclidean embeddings. Furthermore, our method is orthogonal to product quantization, allowing seamless integration to further enhance retrieval systems. We achieve significant improvements in storage efficiency, with scaling potential to larger datasets. The code is provided in the supplementary materials.

1 INTRODUCTION

Compressed representations benefit information retrieval, as they greatly reduce index size, i.e., the memory requirements for data embeddings. Such compact property is desirable where retrieval-by-embedding needs to be fast or performed on large collections. Prior work has shown that considerable speed-ups can be obtained for Euclidean representations through binarization (Cai et al., 2020; Jacob et al., 2018; Kim et al., 2021), or by hashing Wang et al. (2018); Shen et al. (2020); Hoe et al. (2021b) representations on top of a network. These approaches do so by splitting the Euclidean representations into regular grids. In contrast, hyperbolic representations naturally allow for lower-dimensional representations (Long et al., 2020; Ghadimi Atigh et al., 2021; Tseng et al., 2023) due to their compact nature. Such lower-dimensional representations allow retrieval systems for vastly reduced storage and have the potential to scale up. Unfortunately, hyperbolic compactness comes at the cost of hefty computations due to its complex metric (Peng et al., 2021). In this work, we overcome this complexity through binarization, unlocking the full potential of hyperbolic embeddings and pushing the embedding to even lower dimensionality. We show that it is possible to get the best of the fast distance calculations of binary embeddings and the compact representations of hyperbolic embeddings, as shown in Figure 1.

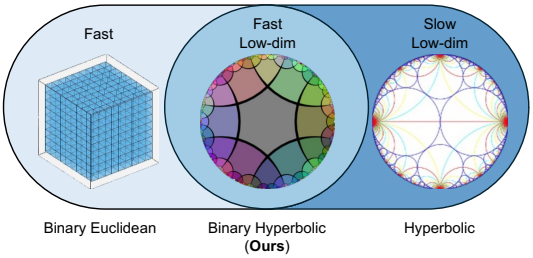

Figure 1: **Binary hyperbolic embeddings** aims the best of both: the fast distance calculations of binary Euclidean embeddings and the compact representations of hyperbolic embeddings.

Hyperbolic deep learning is quickly gaining traction. Primarily, because it allows embedding hierarchies with minimal distortion (Nickel & Kiela, 2017), outperforming Euclidean hierarchical embeddings (Ganea et al., 2018b; Sala et al., 2018). These benefits have been shown for various research problems, from graph networks (Chami et al., 2019; Dai et al., 2021; Liu et al., 2019), reinforcement learning (Cetin et al., 2023) to large language models (Yang et al., 2024; Chen et al., 2024). Specifically, hyperbolic geometry allows for fewer embedding dimensionalities (Liu et al., 2020; Ermolov

et al., 2022; Tseng et al., 2023) and better hierarchical learning (Nickel & Kiela, 2017; Ganea et al., 2018b; Sonthalia & Gilbert, 2020). Despite these advantages, hyperbolic embeddings have not been a viable option for retrieval-by-embedding, as calculating the distance between embeddings involves slow vector operations [1].

This paper introduces supervised binary hyperbolic embedding, a binarization approach that addresses the core limitation of hyperbolic embeddings for retrieval. Our contributions are as follows:

- We unlock the speed potential of hyperbolic embeddings by proving that under retrieval, ~~slow~~ hyperbolic distance computation is ranking preserving to fast Hamming distance computation with our proposed binary encoding.
- Along with the inherent low dimensionality of hyperbolic space, we propose a natural binary hyperbolic embedding, which can obtain even more compacted embedding with substantial speed-up with minimal loss in retrieval performance. Our embedding can be directly used with FAISS (Douze et al., 2024) for immediate memory reduction and speed-up in downstream use.
- We show that these benefits hold across a variety of settings, including the ability to incorporate hierarchical knowledge and the potential to scale to larger retrieval sets.

Our work makes it possible to perform fast search in binarized hyperbolic space, making hyperbolic embeddings a viable supplement for large-scale search and retrieval.

2 Related Work

Since search typically needs to occur on-the-fly (Yuan et al., 2020; Wang et al., 2018) or on huge collections (Jang & Cho, 2021; Chen et al., 2023), it is imperative to efficiently embed queries and data collections. The efficiency of an embedding can be expressed in bits, where fewer bits can ultimately only be obtained in two ways: using fewer embedding dimensions (Cao et al., 2020; Hausler et al., 2021) and/or using fewer bits per dimension (Choukroun et al., 2019; Yao et al., 2022; Bai et al., 2022).

Hyperbolic low-dimensional representations differ from the Euclidean representations for their ability to embed hierarchical structures with minimal distortion Ganea et al. (2018b); Tseng et al. (2023) due to the curved nature of the space Cannon et al. (1997). Most related, a variety of works find that hyperbolic space is naturally low-dimensional (Tifrea et al., 2019; Long et al., 2020; Shimizu et al., 2021; Ghadimi Atigh et al., 2021; Desai et al., 2023; Tseng et al., 2023). Such potential enables dimensionality reduction (Chami et al., 2021; Guo et al., 2022), but at the cost of computational overhead (Shimizu et al., 2021; Peng et al., 2021). In this paper, we exploit the low-dimensional nature, pushing it to fewer bits and turning the computational cost into acceleration.

Low-bit embeddings. For using fewer bits per embedding dimension, classical solutions are given by quantization techniques (Jégou et al., 2011; Jacob et al., 2018), benefiting quantization models designed for large-scale settings (Liu et al., 2021b; Yao et al., 2022). Inspired by these developments, we seek to bring the advantages of low-bit binarization to hyperbolic embeddings.

Binary hashing embeddings (Wang et al., 2017) learn compressed representations into compact binary codes (Shen et al., 2018b; Fan et al., 2020; Hoe et al., 2021b; Shen et al., 2020; Wei et al., 2024) while preserving the semantic similarity (Yuan et al., 2020) or structure (Li & van Gemert, 2021) of the original data, thereby reducing storage and computational costs. Unlike our proposed binarization approach, hashing requires NP-hard optimization and thus demands either complex optimization (Shen et al., 2018a) or substantial relaxation (Wei et al., 2024).

Hyperbolic isometry. There are five isometric models for hyperbolic space (Cannon et al., 1997). We focus on the Poincaré disk model as it is highly suited for binarization; the coordinates on the Poincaré ball are finite, and each axis is symmetric, allowing us to use a simple binarization strategy. Further discussion on the other hyperbolic models can be found in Appendix A.2.

[1] We quantify the slowness of hyperbolic distance $d_{\mathbb{D}}(\cdot,\cdot)$ in Appendix D.

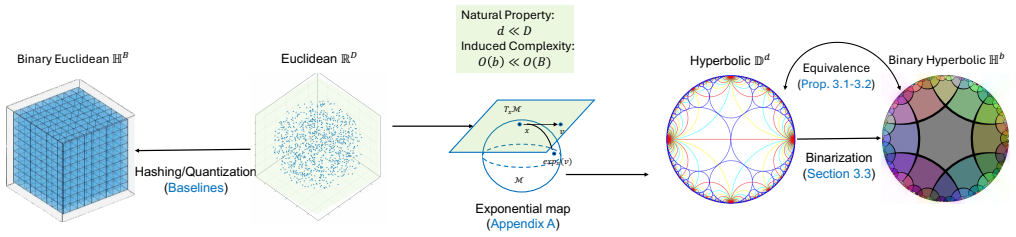

Figure 2: **Overview of our approach.** Where existing baselines perform quantization in Euclidean space (left), we show how to make binarized representations possible in hyperbolic space (right). The main contribution (Propositions 3.1-3.2) highlights the equivalence between hyperbolic embedding $\mathbb{D}^d$ and its corresponding binary hyperbolic embedding $\mathbb{H}^b$. In turn, Section 3.3 details how to make the binarization possible.

Approximate Nearest Neighbor (ANN) search significantly reduces query time for large-scale retrieval (Muja & Lowe, 2014; Douze et al., 2024), where the exact nearest neighbor search is computationally prohibitive. Classical approaches to ANN include tree-based methods (Arya & Mount, 1998), graph-based methods (Malkov & Yashunin, 2018), product quantization based (Jégou et al., 2011; Ge et al., 2014) to balance accuracy and speed. More application-oriented, DiskANN (Subramanya et al., 2019) combines in-memory computation with a disk-resident graph. enabling billion-scale nearest neighbor search on a single machine. In contrast, our approach efficiently performs **exact nearest neighbour search**, by leveraging compact binary hyperbolic embeddings, we avoid the compromises inherent in ANN thus eliminating reliance on distance gap preservation.

3 Binary Hyperbolic Embedding

In this work, we strive to find a binarizer $g(\cdot)$ which encodes real-valued hyperbolic embeddings $\boldsymbol{x}$ into a binary format $\boldsymbol{x}^b$, such that $\boldsymbol{x}^b = g(\boldsymbol{x})$. We do so by constructing an approximate equivalence between hyperbolic distance $\mathrm{d}_{\mathbb{D}}(\cdot,\cdot)$ based search and Hamming distance $\mathrm{d}_{\mathbb{H}}(\cdot,\cdot)$ based search. Then, using the Poincaré model for simplicity, we show how to binarize distances in hyperbolic space[2].

3.1 Problem Statement

Given a query embedding $\boldsymbol{q}$, retrieval is performed through a nearest neighbor search in the database $\mathcal{D}$ that is represented on manifold $\mathcal{M}$:

$$\arg\min_{\boldsymbol{x}\in\mathcal{D}} \mathrm{d}_{\mathcal{M}}(\boldsymbol{q},\boldsymbol{x}). \tag{1}$$

This work argues for hyperbolic geometry as the manifold of choice for retrieval. Its effectiveness, especially in low-dimensional settings, is however offset by the computation complexity of hyperbolic distance $\mathrm{d}_{\mathbb{D}}(\boldsymbol{q},\boldsymbol{x})$ curvature c:

$$\mathrm{d}_{\mathbb{D}}(\boldsymbol{q},\boldsymbol{x}) = \frac{2}{\sqrt{c}}\tanh^{-1}\left(\sqrt{c}\left\|\frac{\left(1-2c\langle\boldsymbol{q},\boldsymbol{x}\rangle+c\|\boldsymbol{x}\|^2\right)\boldsymbol{q}+\left(1-c\|\boldsymbol{q}\|^2\right)\boldsymbol{x}}{1-2c\langle\boldsymbol{q},\boldsymbol{x}\rangle+c^2\|\boldsymbol{q}\|^2\|\boldsymbol{x}\|^2}\right\|^2\right). \tag{2}$$

In this work, we tackle the complexity of hyperbolic metric through binarization of the hyperbolic space as $\boldsymbol{x}^b = g(\boldsymbol{x})$, where we largely benefit from low-dimensional representation while speeding up distance calculations.

Ranking Preservation. To demonstrate the potential of binary hyperbolic embeddings for retrieval, we prove the ranking preservation property between binary hyperbolic embeddings and real-valued hyperbolic embeddings. In other words:

$$\mathrm{d}_{\mathbb{H}}(\boldsymbol{q}^b,\boldsymbol{x}_1^b) \leq \mathrm{d}_{\mathbb{H}}(\boldsymbol{q}^b,\boldsymbol{x}_2^b) \Rightarrow \mathrm{d}_{\mathbb{D}}(\boldsymbol{q},\boldsymbol{x}_1) \leq \mathrm{d}_{\mathbb{D}}(\boldsymbol{q},\boldsymbol{x}_2). \tag{3}$$

In this paper, we connect the Hamming metric to the hyperbolic metric via a (conditioned) ranking preservation between the hyperbolic metric and Euclidean metric on the hyperbolic embeddings.

[2] We provide preliminaries of related hyperbolic properties in Appendix A

3.2 FROM HYPERBOLIC TO HAMMING

We link the hyperbolic distance to the Hamming distance in three steps: (i) we first prove the ranking preservation between hyperbolic and Euclidean metric up under certain conditions, and (ii) using Euclidean metric as a bridge, we show the equivalence between Hamming distance (over binary hyperbolic embeddings) and the hyperbolic distance (over real-valued hyperbolic embeddings).

Proposition 3.1 states that for hyperbolic embeddings, under retrieval conditions, it is possible to produce the same retrieval output between hyperbolic metric $\mathrm{d}_{\mathbb{D}}(\cdot,\cdot)$ and Euclidean metric $\mathrm{d}_{\mathbb{R}}(\cdot,\cdot)$.

Proposition 3.1. *(Ranking Preservation) Given query $\boldsymbol{q} \in \mathbb{D}^d$, For any $\boldsymbol{x}_1, \boldsymbol{x}_2 \in \mathbb{D}^d$ in the database such that $|\|\boldsymbol{x}_1\| - \|\boldsymbol{x}_2\|| = \epsilon$, given the Poincaré disk boundary tolerance margin δ, if $0 \leq \epsilon \leq \delta \frac{\mathrm{d}_{\mathbb{R}}(\boldsymbol{q},\boldsymbol{x}_2)-\mathrm{d}_{\mathbb{R}}(\boldsymbol{q},\boldsymbol{x}_1)}{\mathrm{d}_{\mathbb{R}}(\boldsymbol{q},\boldsymbol{x}_2)}$, then $\mathrm{d}_{\mathbb{R}}(\boldsymbol{q},\boldsymbol{x}_1) \leq \mathrm{d}_{\mathbb{R}}(\boldsymbol{q},\boldsymbol{x}_2)$ implies $\mathrm{d}_{\mathbb{D}}(\boldsymbol{q},\boldsymbol{x}_1) \leq \mathrm{d}_{\mathbb{D}}(\boldsymbol{q},\boldsymbol{x}_2)$.*

Proof. The proof is in Appendix B.2. □

This proposition demonstrates that under the condition $0 \leq \epsilon \leq \delta \frac{\mathrm{d}_{\mathbb{R}}(\boldsymbol{q},\boldsymbol{x}_2)-\mathrm{d}_{\mathbb{R}}(\boldsymbol{q},\boldsymbol{x}_1)}{\mathrm{d}_{\mathbb{R}}(\boldsymbol{q},\boldsymbol{x}_2)}$, the hyperbolic distance produces the same retrieval output as Euclidean distance. It is important to note that the precondition $|\|\boldsymbol{x}_1 - \boldsymbol{x}_2\| = \epsilon \leq \delta \frac{\mathrm{d}_{\mathbb{R}}(\boldsymbol{q},\boldsymbol{x}_2)-\mathrm{d}_{\mathbb{R}}(\boldsymbol{q},\boldsymbol{x}_1)}{\mathrm{d}_{\mathbb{R}}(\boldsymbol{q},\boldsymbol{x}_2)}$ holds not only because normalizing embeddings is a common practice (Radford et al., 2021), but also because the embeddings used in this paper are closely distributed around normalized prototypes (Long et al., 2020; Kasarla et al., 2022).

As a follow-up step, in Proposition 3.2 we prove that under proper binarization $g(\boldsymbol{x}) = \boldsymbol{x}^b$, hyperbolic metric $\mathrm{d}_{\mathbb{D}}(\boldsymbol{x}, \boldsymbol{y})$ yields identical retrieval outputs as Hamming metric $\mathrm{d}_{\mathbb{H}}(\boldsymbol{x}^b, \boldsymbol{y}^b)$:

Proposition 3.2. *(Binary Ranking Preservation) For a binarizer $g(\cdot)$ such that $\langle \mathbf{x}^+, \mathbf{y}^+ \rangle \propto \langle g(\mathbf{x}), g(\mathbf{y}) \rangle$, $\mathrm{d}_{\mathbb{D}}(\mathbf{x}, \mathbf{y})$ yields the same ranking results as to Hamming distance $\mathrm{d}_{\mathbb{H}}(\mathbf{x}^b, \mathbf{y}^b) = \|\mathbf{x}^b \oplus \mathbf{y}^b\|_0$ for nearest neighbor search.*

Proof. The proof is in Appendix B.3. □

Intuitively, the propositions state that a hyperbolic distance-based search generates the same retrieval ordering as a Hamming distance-based search, which can be computed quickly through binary operations. This is exactly the step to make distance-based nearest neighbor search fast in hyperbolic embeddings. Throughout this work, we use the Poincaré ball for our hyperbolic operations due to its widespread use in deep learning (Peng et al., 2021; Mettes et al., 2023), but we note that our approach applies to any hyperbolic model:

Remark 3.3. Under the isometry defined in Cannon et al. (1997), five hyperbolic models yield equivalent retrieval results.

Proof. The proof is in Appendix B.4. □

3.3 BINARY HYPERBOLIC QUANTIZATION

Based on Proposition 3.2, we can perform binary operation-based search while using hyperbolic embeddings. To make this practically operational, we first generate full-precision hyperbolic embeddings on the Poincaré ball by optimizing embedding network $f(\cdot)$ [3] and then binarize the embeddings via quantization.

Binary quantization. With the trained hyperbolic embedding $\boldsymbol{x}$, we perform binary quantization to obtain the binary representation of $\boldsymbol{x}$, denoted as $\boldsymbol{x}^b = g(\boldsymbol{x})$. In this section, we show that by designing a binarizer $g(\cdot)$ such that it satisfies $\langle g(\boldsymbol{x}), g(\boldsymbol{y}) \rangle \propto \langle \boldsymbol{x}, \boldsymbol{y} \rangle$ in a block-wise manner, we can exploit Proposition 3.2 for a binary Hamming distance-based search with hyperbolic embeddings.

In the Poincaré ball model, all dimensions fall in the radius of the ball $(-r, r)$. We shift each dimension by r to make it in the range $(0, 2r)$:

$$\boldsymbol{x}^+ = \boldsymbol{x} + r. \tag{4}$$

[3] Hyperbolic embedding generation is described in Appendix B

This shift simplifies the calculations without changing the Euclidean distance:

$$\begin{aligned} \mathrm{d}_{\mathbb{R}}(\boldsymbol{x}^+, \boldsymbol{y}^+) &= \|\boldsymbol{x}^+ - \boldsymbol{y}^+\| = \|\boldsymbol{x} + r\mathbf{1} - (\boldsymbol{y} + r\mathbf{1})\| \\ &= \|\boldsymbol{x} - \boldsymbol{y}\| = \mathrm{d}_{\mathbb{R}}(\boldsymbol{x}, \boldsymbol{y}). \end{aligned} \tag{5}$$

In our proposed approach, the representation undergoes a dimension-wise quantization process. For n bits used by each dimension, we partition each dimension into a distinct set of $2^n - 1$ quantization levels under the same framework as Jeon et al. (2020) with respect to scale:

$$s = \frac{\sup(\boldsymbol{x}) - \inf(\boldsymbol{x})}{2^n - 1} = \frac{\sup(\boldsymbol{x}^+) - 0}{2^n - 1} = \frac{2r}{2^n - 1}, \tag{6}$$

where $\sup(\cdot)$ is the supremum and $\inf(\cdot)$ is the infimum. Then we can convert each dimension concerning the scale into integers, which can be converted into *n-bits* binary code:

$$\boldsymbol{x}_{\text{int}} = \lfloor \frac{\boldsymbol{x}^+}{s} \rceil = \sum_{i=1}^{n} 2^{n-i} \cdot \boldsymbol{x}_i^b = 2^{n-1} \cdot \boldsymbol{x}_1^b + 2^{n-2}\boldsymbol{x}_2^b + \cdots + 2^0 \boldsymbol{x}_n^b, \tag{7}$$

where $\boldsymbol{x}_i^b \in \{0, 1\}^d$ represent the binary code for i-th significant bits in each dimension of $\boldsymbol{x}_{\text{int}}$.

To relate $\boldsymbol{x}^b$ to $\boldsymbol{x}^+$, we can similarly decompose vector $\boldsymbol{x}$ as a summation of base vectors that correspond to different significant bits[4]:

$$\boldsymbol{x}^+ = \boldsymbol{x}_1^+ + \boldsymbol{x}_2^+ + \cdots + \boldsymbol{x}_n^+.$$

Binary grouping: assuming zero quantization error, we have a **block-wise proportionals**:

$$\begin{aligned} &\langle \mathbf{x}^+, \mathbf{y}^+ \rangle \propto \langle \mathbf{x}_{int}^+, \mathbf{y}_{int}^+ \rangle \\ &\langle \mathbf{x}_1^+, \mathbf{y}_1^+ \rangle \propto \langle \mathbf{x}_1^b, \mathbf{y}_1^b \rangle \\ &\langle \mathbf{x}_2^+, \mathbf{y}_2^+ \rangle \propto \langle \mathbf{x}_2^b, \mathbf{y}_2^b \rangle \\ &\cdots \\ &\langle \mathbf{x}_n^+, \mathbf{y}_n^+ \rangle \propto \langle \mathbf{x}_n^b, \mathbf{y}_n^b \rangle, \end{aligned} \tag{8}$$

which results in:

$$\langle \boldsymbol{x}^+, \boldsymbol{y}^+ \rangle = s^2 \langle \boldsymbol{x}_{\text{int}}, \boldsymbol{y}_{\text{int}} \rangle = 4^{n-1} \cdot \langle \boldsymbol{x}_1^b, \boldsymbol{y}_1^b \rangle + 4^{n-2} \cdot \langle \boldsymbol{x}_2^b, \boldsymbol{y}_2^b \rangle + \cdots + \langle \boldsymbol{x}_n^b, \boldsymbol{y}_n^b \rangle, \tag{9}$$

leading to a **block-wise application** of Proposition 3.2. We can obtain the distance metric for binary hyperbolic embeddings as:

$$\mathrm{d}_{\mathbb{R}}(\boldsymbol{x}, \boldsymbol{y}) = \mathrm{d}_{\mathbb{R}}(\boldsymbol{x}^+, \boldsymbol{y}^+) = d_{\mathbb{H}}^{\Sigma}(\boldsymbol{x}^b, \boldsymbol{y}^b) = \Sigma_{i=1}^{n} 4^{n-i} \cdot \mathrm{d}_{\mathbb{H}}(\boldsymbol{x}_i^b, \boldsymbol{y}_i^b) \tag{10}$$

where $d_{\mathbb{H}}^{\Sigma}(\boldsymbol{x}^b, \boldsymbol{y}^b)$ is a summation of the scaled hamming distance, hence we can use the scaled binary hamming distance as an approximation of the real-valued distance. The scaling only happens on each of the $n - 1$ bits, resulting in $n - 1$ binary bit-shift operations with integer addition, which can be efficiently carried out. Equipped with a hyperbolic embedding network $f(\cdot)$ and binarization $g(\cdot)$, fast retrieval can be performed by embedding the entire database. Then for a query q and search collection S, both embedded to $\mathbb{D}$ and quantized, we can perform fast nearest neighbor search:

$$\arg\min_{\boldsymbol{v} \in S} d_{\mathbb{H}}^{\Sigma}(\boldsymbol{q}^b, \boldsymbol{v}^b) \triangleq \arg\min_{\boldsymbol{v} \in S} \mathrm{d}_{\mathbb{D}}(\boldsymbol{q}, \boldsymbol{v}). \tag{11}$$

4 Experiments

4.1 Experimental Setup

We focus on retrieval in the image and video domains to measure the performance of various embedding compression approaches across a range of compression levels for retrieval performance and speed. hyperbolic LLMs are not included as they are either not yet open-sourced (Chen et al., 2024) or the text embeddings stay in Euclidean space (Yang et al., 2024). The performance is measured

[4]We show a concrete example in Appendix

Table 1: **Comparing manifolds and binarization for retrieval** on CIFAR100, ImageNet1K, and Moments-in-Time. Underlined scores denote best full-precision embedding performance; **bold** scores denote best binary embedding performance. For each manifold, we use the following settings: Euclidean space $\mathbb{R}^D$ (Liu et al., 2021a), hyperspherical space $\mathbb{S}^d$ (Kasarla et al., 2022), and hyperbolic space $\mathbb{D}^d$ (Long et al., 2020). D, d denotes the dimensionality of the real-valued space, and B, b is the binary representation's dimensionality. All retrievals are cut off at 50. With full precision, hyperbolic embeddings already outperform Euclidean embeddings but are slow to evaluate. Our binary hyperbolic embeddings at 512 bits can maintain this performance while being much faster to evaluate, thereby maintaining performance at a much smaller embedding size.

		CIFAR100		ImageNet1K		Moments-in-Time	
Manifold	Embedding size	mAP	SmAP	mAP	SmAP	mAP	SmAP
$\mathbb{R}^D$	16384 bits	0.7938 ±0.0014	0.8868 ±0.0029	0.6324 ±0.0037	0.6879 ±0.0035	0.1598 ±0.0002	0.2371 ±0.0025
$\mathbb{S}^d$	8192 bits	0.8110 ±0.0037	0.8953 ±0.0021	0.6314 ±0.0019	0.6870 ±0.0021	0.1624 ±0.0015	0.2408 ±0.0022
$\mathbb{D}^d$	8192 bits	0.8078 ±0.0015	0.9017 ±0.0014	0.6344 ±0.0011	0.6894 ±0.0010	0.1780 ±0.0001	0.2578 ±0.0019
$\mathbb{R}^B$	1024 bits	0.6127 ±0.0005	0.7827 ±0.0002	0.6299 ±0.0008	0.6840 ±0.0076	0.1387 ±0.0013	0.2080 ±0.0017
$\mathbb{S}^b$	512 bits	0.7943 ±0.0006	0.8847 ±0.0004	0.6320 ±0.0015	0.6863 ±0.0017	0.1584 ±0.0018	0.2303 ±0.0019
$\mathbb{D}^b$ (ours)	512 bits	**0.7948** ±0.0023	**0.9014** ±0.0007	**0.6358** ±0.0018	**0.6992** ±0.0017	**0.1769** ±0.0015	**0.2536** ±0.0018

Table 2: **Integrating Binary Hyperbolic Embeddings in FAISS** on ImageNet1K-val. The results show that we can directly incorporate our approach into FAISS, making for a retrieval method that is strong in performance, with minimal index size, and top retrieval speed.

Embedding	mAP@50 ↑	SmAP@50 ↑	Index Size ↓	Retrieval Speed (s) ↓
Euclidean-512D	0.6324 ±0.0037	0.6879 ±0.0035	102MB	2.83 ± 0.07
Euclidean-256D	0.5847 ±0.0004	0.6374 ±0.0003	51MB	1.11 ± 0.04
Hyperbolic-256D	0.6344 ±0.0011	0.6894 ±0.0010	51MB	1.11 ± 0.06
BinaryHyperbolic-256bit	0.6320 ±0.0014	0.6875 ±0.0015	**1.5MB**	**0.28 ± 0.03**
BinaryEuclidean-512bit	0.5849 ±0.0024	0.6376 ±0.0015	3MB	1.03 ± 0.04
BinaryHyperbolic-512bit	**0.6358** ±0.0006	**0.6992** ±0.0005	3MB	1.04 ± 0.03

with mean average precision (mAP@50) and speed as the relative difference in retrieval time in seconds on the test set.

Datasets. We use three well-studied datasets with optional hierarchical knowledge: CIFAR100, ImageNet1K, and Moments in Time. CIFAR100 comes with an officially defined hierarchy (Krizhevsky et al., 2009), while for ImageNet1K each of the 1,000 object classes is a node in the WordNet hierarchy (Miller, 1995).In Moments in Time, each of the 339 classes is a node in the VerbNet hierarchy (Schuler, 2006). We also examine the large-scale Quick Draw dataset (Google, 2023), which contains 50 million sketch images from 345 categories. There is no hierarchy in Quick Draw, hence we use a simple hierarchy that all categories belong to a super-class *root*.

Implementation details. For hyperbolic prototpes learning, we use a curvature of $c = 0.1$ and the Riemannian Adam optimizer (Becigneul & Ganea, 2019), supported by the *geoopt* (Kochurov et al., 2020) with a learning rate 10^{-4}. In practice, when learning hyperbolic embeddings based on hyperbolic prototypes, Riemannian Adam can be replaced by Adam as the learnable parameters are in Euclidean space. Unless specified otherwise, we report supervised results on hyperbolic embeddings with hierarchical prototypes. All experiments were performed on a single Nvidia A6000 GPU. For the image experiments, we use the Swin (Liu et al., 2021a) on 32×32 patches for CIFAR-100 and ImageNet1K. For the video experiments, we use a pre-trained 3D Swin (Liu et al., 2022).

Evaluation. For a fair comparison, the same frozen backbone is used across all competing models. Unless stated otherwise, we use two bits per dimension for binarization following Hubara et al. (2018). To measure the speed-up, we perform both FAISS-based evaluation and purpose-made stand-alone experiments for measuring the retrieval speed. Note that Speed-up relies on the implementation in the mathematical library used. For example, a boolean variable in Pytorch is treated as an 8-bit unsigned int, which does not accurately reflect speed-up. Therefore, in addition to FAISS, we use a C++ implementation that supports vectorized float&bitwise operations to evaluate the speed-up. All speed-ups are relative to 512-dimensional full-precision Euclidean representation.

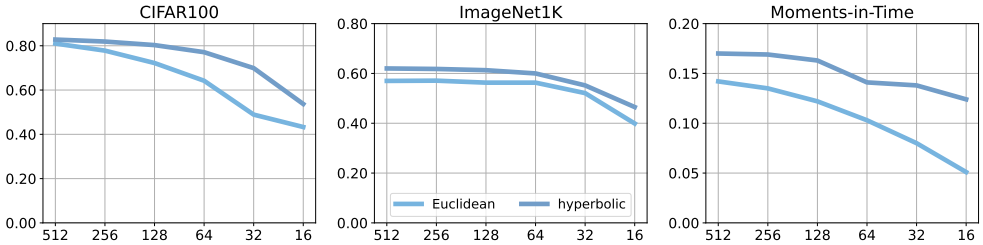

Figure 3: **Retrieval performance (mAP@50) as a function of bits** on CIFAR100, ImageNet1K, and Moments-in-Time. Binary hyperbolic embeddings allow for strong compression while maintaining performance, especially in low-bit settings.

4.2 Binary versus non-binary retrieval

We first investigate the effect of manifold and binarization on retrieval performance and speed. For binarized embeddings, we use 512 bits and report the results for mAP@50. As our proof in Equation 11 shows that our binarization-based similarity is equivalent to the similarity in $\mathbb{R}$ and $\mathbb{D}$, we can use the same binarization strategy across all three manifolds: Euclidean $\mathbb{R}$, hyperspherical $\mathbb{S}$, and hyperbolic $\mathbb{D}$. For all, we use the same frozen backbone with a linear projection on top, supervised by the retrieval task, to get features with the same dimensionality. The Euclidean baseline follows conventional cross-entropy optimization, while the hyperspherical baseline uses maximally separate prototypes (Kasarla et al., 2022) optimized with cosine similarity between all prototype pairs. The hyperbolic embedding is trained akin to Long et al. (2020).

The results in Table 1 show that for full-precision embeddings, hyperbolic space shows great promise for retrieval, outperforming its Euclidean and hyperspherical alternatives. However, hyperbolic embedding retrieval is five times slower than Euclidean retrieval. With binary hyperbolic embeddings, we are able to induce a large speed-up with the highest retrieval scores. On ImageNet1K, we obtain a mAP@50 of 63.44% compared to 63.24% and 63.14% for the Euclidean and hyperspherical baselines. We find that hyperbolic embeddings retain more performance when binarized, highlighting the strong match between hyperbolic space and binarization. Results in Table 2 also show its effectiveness when combined with FAISS. Results show that binarization on hyperbolic embeddings is preferred for retrieval.

4.3 Effect of bit length and quantization level

Effect of bit length. A recurring theme in recent hyperbolic learning papers is the potential of low-dimensional effectiveness (Long et al., 2020; Ermolov et al., 2022; Ghadimi Atigh et al., 2021). To explore the impact of low-dimensional embeddings for fast retrieval, we performed an experiment where we compare Euclidean to hyperbolic embeddings as a function of the number of used bits on all three datasets. For both baselines, we investigate using 512, 256, 128, and 64 bits, corresponding to 256-, 128-, 64-, and 32-dimensional embedding dimensions.

The results of the bit length comparison are shown in Figure 4.3. The trade-off between embedding dimensions and quantization levels on ImageNet1K. Larger, darker bubbles represent configurations with more bits and better mAP but slower speed. The baseline is 512d x 32 bits with an mAP of 0.6344 and no speedup (1x).

Table 3: **The Trade of embedding dimensions and quantization bits** on ImageNet1K. Underlined scores denote full-precision. With binary hyperbolic embeddings, we obtain substantial acceleration with roughly the same performance. The speed-up is based on Integrating our embedding in Faiss. Another C++ version speed-up analysis is in Figure 4.3

$dim \times bits$	mAP@50 ↑	Speed(s) ↓
8 ×2	0.1641 ±0.0011	0.46 ±0.03
8 ×4	0.1384 ±0.0005	0.22 ±0.08
16 ×2	0.2832 ±0.0008	**0.17** ±0.02
16 ×4	0.2745 ±0.0009	0.18 ±0.02
32 ×2	0.4817 ±0.0072	0.18 ±0.02
32 ×4	0.4479 ±0.0079	0.22 ±0.02
64 ×2	0.5814 ±0.0104	0.21 ±0.02
64 ×4	0.5968 ±0.0022	0.21 ±0.01
128×2	0.6365 ±0.0067	0.28 ±0.02
128×4	0.6320 ±0.0014	1.03 ±0.04
256×2	**0.6358** ±0.0006	1.00 ±0.02
512×32	0.6344±0.0036	2.83 ±0.07

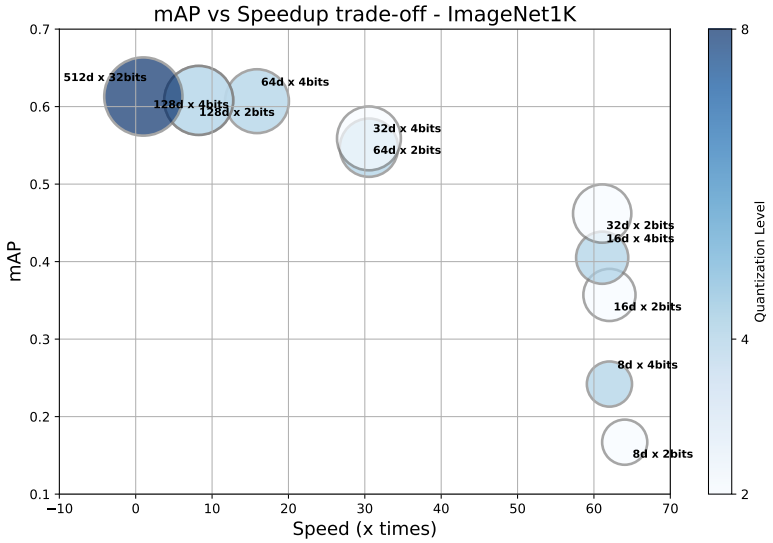

Figure 4: **The effect of embedding dimensions and quantization bits** on ImageNet1K-Val. The darkest bubble denotes the full-precision Euclidean embedding. With binary hyperbolic embeddings, we can obtain significant ($\sim 8\times$) accerlation at roughly the same performance.

Smaller, lighter bubbles show faster configurations, like 128d x 2 bits, achieving 16x speedup with an mAP of 0.6365. The figure illustrates that binary hyperbolic embeddings offer significant speedup (up to 8x) while maintaining comparable performance to the full-precision baseline.

Effect of quantization level. By quantizing each dimension into levels we can choose the bits per dimension. The total number of bits can therefore be determined by using more embedding dimensions with few bits or vice versa. For example, a 128-bit embedding can be obtained from a 64-dimensional embedding with 2 bits per dimension, or a 32-dimensional embedding with 4 bits per dimension. In Table 3, we show the impact across multiple choices of bit sizes. Overall, we find that it is beneficial to use more embedding dimensions with stronger compression than the other way around. This indicates that there is more information in any additional dimension compared to the additional precision within a dimension. We show more comparisons of other datasets in Appendix D.1. The speed-up results in Table 3 paint a clear picture: the speed-up can be obtained without hampering retrieval performance. Our approach allows for much bigger speed-up, but high compression then comes at the price of lower retrieval performance, making it a design choice how to balance both.

4.4 Effect of hierarchical knowledge

A key benefit of hyperbolic space is the capability to embed hierarchical knowledge with minimal distortion for hierarchical embeddings (Ganea et al., 2018b; Sala et al., 2018). Such property enables a hyperbolic network to retrieve semantically similar items of adjacent classes (Long et al., 2020), Following which setting, in Appendix D.2 we report results with hierarchical knowledge-aware retrieval. We can maintain retrieval performance in both standard and hierarchy-aware settings. Even with the lowest number of bit lengths.

Qualitative analysis. In Figure 5 we compare a non-hierarchical spherical space with our hierarchical hyperbolic space. All classes are connected to classes with pairwise cosine similarity greater than 0.5. To measure the similarity between classes we average the embeddings for all instances of a class, reducing it to pair-wise relationships. The figure shows that we are better at organizing concepts hierarchically, which as a consequence means that inputs with hierarchically similar concepts

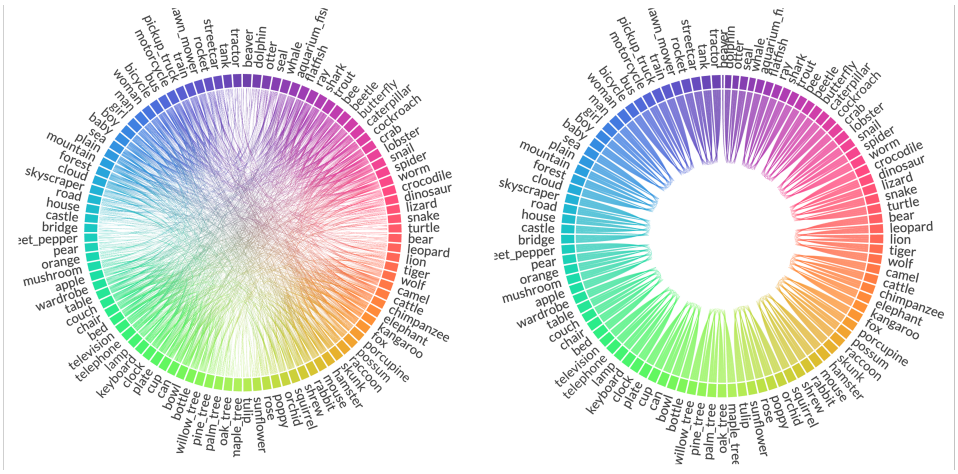

Figure 5: **Visualization of pair-wise class similarities** for (left) non-hierarchical spherical embeddings and (right) our hierarchical binary embeddings. Our embeddings are organized more hierarchically, balancing strong quantization and hierarchical performance.

Table 4: **The effect of curvature** on CIFAR100. Parameter r^2 is the squared radius used when constructing the class prototypes $\boldsymbol{P}$ on poincaré disk, whereas c is the curvature used when optimizing $f(\cdot)$ to map data samples to class prototypes. Low curvature indicates nearly uncurved, Euclidean-like space, where high curvature causes numerical instability. Hence a middle ground for class prototype embedding and sample embedding is preferred.

	$r^2 = 10^3$	$r^2 = 10^2$	$r^2 = 10$	$r^2 = 1$	$r^2 = 0.1$
$c = 10^{-3}$	0.7045 $\pm$0.0027	0.7294 $\pm$0.0021	0.7930 $\pm$0.0029	0.7810 $\pm$0.0031	0.7921 $\pm$0.0018
$c = 10^{-2}$	-	0.7889 $\pm$0.0024	0.7939 $\pm$0.0029	<u>0.7947</u> $\pm$0.0025	0.7896 $\pm$0.0019
$c = 0.1$	-	-	0.7938 $\pm$0.0030	**0.7948** $\pm$0.0023	0.7938 $\pm$0.0021
$c = 1$	-	-	-	0.7463 $\pm$0.0015	0.7817 $\pm$0.0020
$c = 10$	-	-	-	-	0.5627 $\pm$0.0013

are more likely to fall in the same quantization bin. This enables better hierarchical performance even at low bit length. We suspect this is because spherical embeddings are learned by forcing classes to be equally dissimilar, whereas in hyperbolic space we can enforce a margin between classes while keeping track of siblings due to its infinite boundary nature.

4.5 Effect of Curvature and Radius

The curvature of the Poincaré disk model is determined by c; r controls the radius for constructing prototypes (optionally with the hierarchy $\mathcal{H}$) $\boldsymbol{p}_i$, with which we learn $f(\cdot)$ to map the input samples to the class prototypes. Meanwhile, c is the curvature of $\mathbb{D}$ where we embed images and videos, it can be regarded as adjusting the hyperbolic metric, resulting in a different distance calculation with the same prototypes. In Table 4 we compare different settings for c and r and find an interaction between the two parameters, with the highest performance obtained with a high r and a low c. Overall, training class prototypes with an intermediate curvature is preferred, we suspect that is because the class prototypes are not pushed to the disk boundary, thereby leaving some room for embedding class instances in the later stage. More analyses of other datasets are given in Appendix D.3.

4.6 Quantization and Large-Scale Comparisons

Both our method and classical product quantization can be regarded as post-processing on top of existing feature vectors. We draw a comparison in Table 5. Besides its superior performance, we find, interestingly, if we combine our method with PQ, i.e., using the binary hyperbolic embeddings

Table 5: **Comparison and combination with product quantization.** Product quantization is a canonical approach in retrieval, but not competitive to our binary hyperbolic embeddings in either the unsupervised or the supervised setting.

	CIFAR100			ImageNet1K-Val		
	128bit	256bit	512bit	128bit	256bit	512bit
Unsupervised PQ (Jégou et al., 2011)	0.5213 ± 0.0009	0.5372 ± 0.0012	0.5503 ± 0.0015	0.3574 ± 0.0016	0.4152 ± 0.0018	0.4573 ± 0.0021
Unsupervised Ours	0.5304 ± 0.0011	0.5412 ± 0.0013	0.5497 ± 0.0016	0.3736 ± 0.0015	0.4213 ± 0.0019	0.4584 ± 0.0020
$\mathbb{D}$ + PQ (Jégou et al., 2011)	0.7102 ± 0.0019	0.7304 ± 0.0022	0.7353 ± 0.0025	0.5452 ± 0.0029	0.6051 ± 0.0030	0.6082 ± 0.0031
$\mathbb{D}$ + OPQ (Ge et al., 2014)	0.7613 ± 0.0018	0.7714 ± 0.0020	0.7782 ± 0.0021	0.5681 ± 0.0025	0.6212 ± 0.0032	0.6213 ± 0.0030
Ours + OPQ	0.7747 ± 0.0016	0.7726 ± 0.0012	0.7814 ± 0.0026	$0.xxxx \pm 0.0025$	$0.xxxx \pm 0.0032$	$0.xxxx \pm 0.0030$
Ours	$\mathbf{0.8031} \pm 0.0010$	$\mathbf{0.8090} \pm 0.0040$	$\mathbf{0.8177} \pm 0.0030$	$\mathbf{0.5814} \pm 0.0104$	$\mathbf{0.6365} \pm 0.0067$	$\mathbf{0.6358} \pm 0.0006$

as the feature vectors for PQ, it further improves the performance of PQ. This might be because our binary grouping in eq equation 8 already groups each group of sub-space, thus better aligned with PQ's subspace division. We furthermore compare to hashing methods, which require a long training time and are not easily scalable to large datasets. As a result, recent hashing research has focused on small datasets for validation. Therefore, in this paper, due to the outsized training cost, we do not compare the performance of hashing methods on large datasets. In Table 6, we show that on CIFAR-100, our approach is on par with the hashing methods, while we do not require complex optimization and our performance does not decrease after as bit-length goes beyond 128.

Table 6: **Comparison to hashing methods** on CIFAR-100 Our approach is preferred, without incurring complex optimization, while the performance kept increasing without being limited to a high number of bits.

	16bits	32bits	64bits	128bits	512bits
CSQ (Yuan et al., 2020)	0.6473 ± 0.003	$\mathbf{0.7562} \pm 0.002$	$\mathbf{0.7981} \pm 0.001$	0.8101 ± 0.002	0.8072 ± 0.002
DPN (Fan et al., 2020)	0.6370 ± 0.004	0.7431 ± 0.003	0.7902 ± 0.002	0.8090 ± 0.002	0.8130 ± 0.003
OrthoCos (Hoe et al., 2021a)	0.6630 ± 0.004	0.7552 ± 0.003	0.7905 ± 0.003	$\mathbf{0.8120} \pm 0.002$	0.8012 ± 0.002
BiHalf (Li & van Gemert, 2021)	0.6775 ± 0.003	0.7572 ± 0.002	0.7887 ± 0.002	0.7977 ± 0.001	0.7803 ± 0.002
Hyperbolic-Hashing (Yu et al., 2024)	0.2490 ± 0.012	0.3921 ± 0.009	0.4893 ± 0.008	0.5693 ± 0.007	0.6013 ± 0.002
Ours	0.5370 ± 0.002	0.6990 ± 0.001	0.7706 ± 0.005	0.8031 ± 0.001	$\mathbf{0.8177} \pm 0.003$

To showcase the potential of our approach on large-scale settings, we also experiment on the Quick Draw dataset (Google, 2023). Here, we embed the raw 50 Million images with a simple MLP backbone followed by a Euclidean or hyperbolic head. To avoid out-of-memory issues, we use 64 embedding dimensions, and 4-bit quantization and perform retrieval on two randomly picked query sets (one small scale and one large scale) of the test set. The results in Table 7 show that on such large-scale settings, binary hyperbolic embeddings remain highly effective.

Table 7: **Large-scale evaluation on QuickDraw**, demonstrating that binary hyperbolic embeddings are scalable as well.

	QuickDraw-50K	**QuickDraw-10M**
Euclidean Binarization	0.2445	0.0407
Ours	**0.3149**	**0.0712**

5 Conclusion

Hyperbolic deep learning has a wide range of applications, from images to videos. However, its application in large-scale search has been hampered by slow distance calculations. In this work, we overcome this limitation by proving the retrieval equivalence between hyperbolic and Hamming distances, which allows binarization of the hyperbolic space and significantly accelerates distance calculations. We experimentally verify this acceleration, across the video and image domain, obtaining significant accerlation at roughly equal performance. Our hyperbolic binary embeddings demonstrate the viability of hyperbolic space for large-scale retrieval and hierarchical retrieval.

Broader impact. The proposed model, through binarization of hyperbolic space, substantially decreases memory consumption and computational costs for retrieval, which contributes to reducing energy costs and infrastructure expenses.

Limitations. A limitation of hyperbolic embeddings on a Poincaré disk is the issue of numerical stability (Yu & De Sa, 2019; Mishne et al., 2023), as it relies on a finite numerical range to represent an infinite volume. This constraint becomes particularly pronounced because the Poincaré disk model compresses distances exponentially as they approach the boundary, leading to substantial precision challenges. An induced limitation is that we binarize the embeddings uniformly in a non-uniform space, which would be an inspiration for future work. Double-precision arithmetic is recommended to mitigate numerical instabilities near the disk's edge.

REFERENCES

Sunil Arya and David M Mount. An optimal algorithm for approximate nearest neighbor searching in fixed dimensions. Journal of the ACM (JACM), 45(6):891–923, 1998.

Mina Ghadimi Atigh, Julian Schoep, Erman Acar, Nanne van Noord, and Pascal Mettes. Hyperbolic image Segmentation. In 2020 IEEE/CVF Conference on Computer Vision and Pattern Recognition, pp. 4453–4462, 2022.

Haoli Bai, Lu Hou, Lifeng Shang, Xin Jiang, Irwin King, and Michael R. Lyu. Towards Efficient Post-training Quantization of Pre-trained Language Models. In Advances in Neural Information Processing Systems, pp. 1405–1418, 2022.

Ivana Balazevic, Carl Allen, and Timothy Hospedales. Multi-relational Poincaré Graph Embeddings. In Advances in Neural Information Processing Systems, 2019.

Bjorn Barz and Joachim Denzler. Deep Learning on Small Datasets without Pre-Training using Cosine Loss. In IEEE Winter Conference on Applications of Computer Vision, pp. 1371–1380, 2020.

Gary Becigneul and Octavian-Eugen Ganea. Riemannian adaptive optimization methods. In International Conference on Learning Representations, 2019.

Yaohui Cai, Zhewei Yao, Zhen Dong, Amir Gholami, Michael W. Mahoney, and Kurt Keutzer. ZeroQ: A Novel Zero Shot Quantization Framework. In 2020 IEEE/CVF Conference on Computer Vision and Pattern Recognition, pp. 13169–13178, 2020.

James W Cannon, William J Floyd, Richard W Kenyon, and Walter R Parry. Hyperbolic geometry. In Flavors of Geometry, pp. 59–115, 1997.

Bingyi Cao, André Araujo, and Jack Sim. Unifying Deep Local and Global Features for image search. In European Conference on Computer Vision, pp. 726–743, 2020.

Edoardo Cetin, Benjamin Chamberlain, Michael Bronstein, and Jonathan J Hunt. Hyperbolic deep reinforcement learning. In International Conference on Learning Representations, 2023.

Ines Chami, Zhitao Ying, Christopher Ré, and Jure Leskovec. Hyperbolic graph convolutional neural networks. In Advances in neural information processing systems, 2019.

Ines Chami, Albert Gu, Dat P. Nguyen, and Christopher Re. HoroPCA: Hyperbolic Dimensionality Reduction via Horospherical Projections. In Proceedings of the 38th International Conference on Machine Learning, pp. 1419–1429, 2021.

Wei Chen, Yu Liu, Weiping Wang, Erwin M. Bakker, Theodoros Georgiou, Paul Fieguth, Li Liu, and Michael S. Lew. Deep learning for instance retrieval: A survey. IEEE Transactions on Pattern Analysis and Machine Intelligence, pp. 7270–7292, 2023.

Weize Chen, Xu Han, Yankai Lin, Kaichen He, Ruobing Xie, Jie Zhou, Zhiyuan Liu, and Maosong Sun. Hyperbolic pre-trained language model. IEEE/ACM Transactions on Audio, Speech, and Language Processing, 2024.

Yoni Choukroun, Eli Kravchik, Fan Yang, and Pavel Kisilev. Low-bit Quantization of neural networks for Efficient Inference. In 2019 IEEE/CVF International Conference on Computer Vision Workshop (ICCVW), pp. 3009–3018, 2019.

Jindou Dai, Yuwei Wu, Zhi Gao, and Yunde Jia. A hyperbolic-to-hyperbolic graph convolutional network. In Computer Vision and Pattern Recognition, 2021.

Karan Desai, Maximilian Nickel, Tanmay Rajpurohit, Justin Johnson, and Shanmukha Ramakrishna Vedantam. Hyperbolic Image-text Representations. In Proceedings of the 40th International Conference on Machine Learning, pp. 7694–7731. PMLR, July 2023. ISSN: 2640-3498.

Matthijs Douze, Alexandr Guzhva, Chengqi Deng, Jeff Johnson, Gergely Szilvasy, Pierre-Emmanuel Mazaré, Maria Lomeli, Lucas Hosseini, and Hervé Jégou. The faiss library. arXiv preprint arXiv:2401.08281, 2024.

Aleksandr Ermolov, Leyla Mirvakhabova, Valentin Khrulkov, Nicu Sebe, and Ivan Oseledets. Hyperbolic vision Transformers: Combining Improvements in Metric Learning. In 2022 IEEE/CVF Conference on Computer Vision and Pattern Recognition (CVPR), pp. 7399–7409, 2022.

Lixin Fan, Kam Woh Ng, Ce Ju, Tianyu Zhang, and Chee Seng Chan. Deep Polarized Network for Supervised Learning of Accurate Binary Hashing Codes. In Proceedings of the Twenty-Ninth International Joint Conference on Artificial Intelligence, pp. 825–831, 2020.

Octavian Ganea, Gary Bécigneul, and Thomas Hofmann. Hyperbolic neural networks. Advances in Neural Information Processing Systems, 2018a.

Octavian Ganea, Gary Becigneul, and Thomas Hofmann. Hyperbolic Entailment Cones for Learning Hierarchical Embeddings. In Proceedings of the 35th International Conference on Machine Learning, pp. 1646–1655, 2018b.

Tiezheng Ge, Kaiming He, Qifa Ke, and Jian Sun. Optimized product quantization. IEEE transactions on pattern analysis and machine intelligence, 36(4):744–755, 2014.

Mina Ghadimi Atigh, Martin Keller-Ressel, and Pascal Mettes. Hyperbolic Busemann Learning with Ideal Prototypes. In Advances in Neural Information Processing Systems, pp. 103–115, 2021.

Google. Quick, draw! dataset, 2023. URL `https://github.com/googlecreativelab/quickdraw-dataset`.

Yunhui Guo, Haoran Guo, and Stella X Yu. Co-sne: Dimensionality reduction and visualization for hyperbolic data. In Proceedings of the IEEE/CVF Conference on Computer Vision and Pattern Recognition, pp. 21–30, 2022.

Stephen Hausler, Sourav Garg, Ming Xu, Michael Milford, and Tobias Fischer. Patch-netvlad: Multi-scale fusion of locally-global descriptors for place recognition. In 2021 IEEE/CVF Conference on Computer Vision and Pattern Recognition (CVPR), pp. 14136–14147, 2021.

Jiun Tian Hoe, Kam Woh Ng, Tianyu Zhang, Chee Seng Chan, Yi-Zhe Song, and Tao Xiang. One loss for all: Deep hashing with a single cosine similarity based learning objective. Advances in Neural Information Processing Systems, 34:24286–24298, 2021a.

Jiun Tian Hoe, Kam Woh Ng, Tianyu Zhang, Chee Seng Chan, Yi-Zhe Song, and Tao Xiang. One Loss for All: Deep Hashing with a Single Cosine Similarity based Learning Objective. In Advances in Neural Information Processing Systems, pp. 24286–24298, 2021b.

Itay Hubara, Matthieu Courbariaux, Daniel Soudry, Ran El-Yaniv, and Yoshua Bengio. Quantized neural networks: Training neural networks with Low Precision Weights and Activations. Journal of Machine Learning Research, pp. 1–30, 2018.

Benoit Jacob, Skirmantas Kligys, Bo Chen, Menglong Zhu, Matthew Tang, Andrew Howard, Hartwig Adam, and Dmitry Kalenichenko. Quantization and Training of neural networks for Efficient Integer-Arithmetic-Only Inference. In 2018 IEEE/CVF Conference on Computer Vision and Pattern Recognition, pp. 2704–2713, 2018.

Young Kyun Jang and Nam Ik Cho. Self-Supervised Product Quantization for Deep Unsupervised image Retrieval. In 2019 IEEE/CVF International Conference on Computer Vision (ICCV), pp. 12085–12094, 2021.

Hervé Jégou, Matthijs Douze, and Cordelia Schmid. Product quantization for nearest neighbor search. In IEEE Transactions on Pattern Analysis and Machine Intelligence, volume 33, pp. 117–128. IEEE, 2011.

Yongkweon Jeon, Baeseong Park, Se Jung Kwon, Byeongwook Kim, Jeongin Yun, and Dongsoo Lee. BiQGEMM: Matrix Multiplication with Lookup Table for Binary-Coding-Based Quantized DNNs. In SC20: International Conference for High Performance Computing, Networking, Storage and Analysis, pp. 1–14, 2020.

H Jégou, M Douze, and C Schmid. Product quantization for nearest neighbor search. IEEE Transactions on Pattern Analysis and Machine Intelligence, pp. 117–128, 2011.

Tejaswi Kasarla, Gertjan Burghouts, Max van Spengler, Elise van der Pol, Rita Cucchiara, and Pascal Mettes. Maximum Class Separation as Inductive Bias in One Matrix. Advances in Neural Information Processing Systems, pp. 19553–19566, 2022.

Valentin Khrulkov, Leyla Mirvakhabova, Evgeniya Ustinova, Ivan Oseledets, and Victor Lempitsky. Hyperbolic image embeddings. In Proceedings of the IEEE/CVF conference on computer vision and pattern recognition, pp. 6418–6428, 2020.

Sehoon Kim, Amir Gholami, Zhewei Yao, Michael W. Mahoney, and Kurt Keutzer. I-BERT: Integer-only BERT Quantization. In Proceedings of the 38th International Conference on Machine Learning, pp. 5506–5518, 2021.

Max Kochurov, Rasul Karimov, and Serge Kozlukov. Geoopt: Riemannian optimization in pytorch, 2020.

Alex Krizhevsky, Vinod Nair, and Geoffrey Hinton. Cifar-100 (canadian institute for advanced research), 2009.

Christopher Lang, Alexander Braun, Lars Schillingmann, and Abhinav Valada. On hyperbolic embeddings in object detection. In DAGM German Conference on Pattern Recognition, pp. 462–476, 2022.

Yunqiang Li and Jan van Gemert. Deep unsupervised image hashing by maximizing bit entropy. In Proceedings of the AAAI Conference on Artificial Intelligence, pp. 2002–2010, 2021.

Qi Liu, Maximilian Nickel, and Douwe Kiela. Hyperbolic graph neural networks. Advances in neural information processing systems, 2019.

Shaoteng Liu, Jingjing Chen, Liangming Pan, Chong-Wah Ngo, Tat-Seng Chua, and Yu-Gang Jiang. Hyperbolic Visual Embedding Learning for Zero-Shot recognition. In 2020 IEEE/CVF Conference on Computer Vision and Pattern Recognition, pp. 9273–9281, 2020.

Ze Liu, Yutong Lin, Yue Cao, Han Hu, Yixuan Wei, Zheng Zhang, Stephen Lin, and Baining Guo. Swin transformer: Hierarchical vision transformer using shifted windows. In Proceedings of the IEEE/CVF international conference on computer vision, pp. 10012–10022, 2021a.

Ze Liu, Jia Ning, Yue Cao, Yixuan Wei, Zheng Zhang, Stephen Lin, and Han Hu. Video swin transformer. In Proceedings of the IEEE/CVF conference on computer vision and pattern recognition, pp. 3202–3211, 2022.

Zhenhua Liu, Yunhe Wang, Kai Han, Wei Zhang, Siwei Ma, and Wen Gao. Post-Training Quantization for vision Transformer. In Advances in Neural Information Processing Systems, pp. 28092–28103, 2021b.

Teng Long, Pascal Mettes, Heng Tao Shen, and Cees G. M. Snoek. Searching for actions on the hyperbole. In 2020 IEEE/CVF Conference on Computer Vision and Pattern Recognition (CVPR), pp. 1138–1147, 2020.

Yury A Malkov and Dmitry A Yashunin. Efficient and robust approximate nearest neighbor search using hierarchical navigable small world graphs. IEEE Transactions on Pattern Analysis and Machine Intelligence, 42(4):824–836, 2018.

Pascal Mettes, Mina Ghadimi Atigh, Martin Keller-Ressel, Jeffrey Gu, and Serena Yeung. Hyperbolic deep learning in computer vision: A survey. arXiv, 2023.

George A Miller. Wordnet: a lexical database for english. Communications of the ACM, 38(11): 39–41, 1995.

Gal Mishne, Zhengchao Wan, Yusu Wang, and Sheng Yang. The Numerical Stability of Hyperbolic Representation Learning. In Proceedings of the 40th International Conference on Machine Learning, 2023.

Antonio Montanaro, Diego Valsesia, and Enrico Magli. Rethinking the compositionality of point clouds through regularization in the hyperbolic space. Advances in Neural Information Processing Systems, 35:33741–33753, December 2022.

Marius Muja and David G Lowe. Scalable nearest neighbor algorithms for high dimensional data. IEEE Transactions on Pattern Analysis and Machine Intelligence, 36(11):2227–2240, 2014.

Alessandro Muscoloni, Josephine Maria Thomas, Sara Ciucci, Ginestra Bianconi, and Carlo Vittorio Cannistraci. Machine learning meets complex networks via coalescent embedding in the hyperbolic space. Nature Communications, pp. 1615, 2017.

Maximillian Nickel and Douwe Kiela. Poincaré Embeddings for Learning Hierarchical Representations. In Advances in Neural Information Processing Systems, 2017.

Zhe Pan and Peng Wang. Hyperbolic Hierarchy-Aware Knowledge Graph Embedding for Link Prediction. In Findings of the Association for Computational Linguistics: EMNLP 2021, pp. 2941–2948, 2021.

Wei Peng, Jingang Shi, Zhaoqiang Xia, and Guoying Zhao. Mix Dimension in Poincaré Geometry for 3D Skeleton-based Action Recognition. In Proceedings of the 28th ACM International Conference on Multimedia, MM '20, pp. 1432–1440. Association for Computing Machinery, October 2020.

Wei Peng, Tuomas Varanka, Abdelrahman Mostafa, Henglin Shi, and Guoying Zhao. Hyperbolic deep neural networks: A survey. IEEE Transactions on Pattern Analysis and Machine Intelligence, 2021.

Alec Radford, Jong Wook Kim, Chris Hallacy, Aditya Ramesh, Gabriel Goh, Sandhini Agarwal, Girish Sastry, Amanda Askell, Pamela Mishkin, Jack Clark, Gretchen Krueger, and Ilya Sutskever. Learning Transferable Visual Models From Natural Language Supervision. In Proceedings of the 38th International Conference on Machine Learning, pp. 8748–8763, 2021.

Frederic Sala, Chris De Sa, Albert Gu, and Christopher Ré. Representation tradeoffs for hyperbolic embeddings. In International conference on machine learning, 2018.

Ramit Sawhney, Harshit Joshi, Rajiv Ratn Shah, and Lucie Flek. Suicide Ideation Detection via Social and Temporal User Representations using Hyperbolic Learning. In Proceedings of the 2021 Conference of the North American Chapter of the Association for Computational Linguistics: Human Language Technologies, pp. 2176–2190, 2021.

Karin Kipper Schuler. VerbNet: A Broad-Coverage, Comprehensive Verb Lexicon. PhD thesis, University of Pennsylvania, 2006.

Fumin Shen, Yan Xu, Li Liu, Yang Yang, Zi Huang, and Heng Tao Shen. Unsupervised deep hashing with similarity-adaptive and discrete optimization. IEEE transactions on pattern analysis and machine intelligence, 40(12):3034–3044, 2018a.

Fumin Shen, Yan Xu, Li Liu, Yang Yang, Zi Huang, and Heng Tao Shen. Unsupervised Deep Hashing with Similarity-Adaptive and Discrete Optimization. IEEE Transactions on Pattern Analysis and Machine Intelligence, pp. 3034–3044, 2018b.

Yuming Shen, Jie Qin, Jiaxin Chen, Mengyang Yu, Li Liu, Fan Zhu, Fumin Shen, and Ling Shao. Auto-Encoding Twin-Bottleneck Hashing. In 2020 IEEE/CVF Conference on Computer Vision and Pattern Recognition, pp. 2818–2827, 2020.

Ryohei Shimizu, Yusuke Mukuta, and Tatsuya Harada. Hyperbolic neural networks++. In International Conference on Learning Representations, 2021.

Rishi Sonthalia and Anna Gilbert. Tree! I am no Tree! I am a low dimensional Hyperbolic Embedding. In Advances in Neural Information Processing Systems, pp. 845–856, 2020.

Akhil G Subramanya, Shravan Kumar, Anshumali Prakash, Anshumali Shrivastava, Andreas Volanakis, Chaitanya Tewari, and Dushyant Singh. Diskann: Fast accurate billion-point nearest neighbor search on a single node. In Advances in Neural Information Processing Systems (NeurIPS), pp. 13765–13775, 2019.

Alexandru Tifrea, Gary Becigneul, and Octavian-Eugen Ganea. Poincare glove: Hyperbolic word embeddings. In International Conference on Learning Representations, 2019.

Albert Tseng, Tao Yu, Toni Liu, and Christopher M. De Sa. Coneheads: Hierarchy Aware Attention. Advances in Neural Information Processing Systems, 36:51421–51433, 2023.

Jingdong Wang, Ting Zhang, Nicu Sebe, and Heng Tao Shen. A survey on learning to hash. IEEE transactions on pattern analysis and machine intelligence, 40(4):769–790, 2017.

Jingdong Wang, Ting Zhang, jingkuan song, Nicu Sebe, and Heng Tao Shen. A Survey on Learning to Hash. IEEE Transactions on Pattern Analysis and Machine Intelligence, pp. 769–790, 2018.

Sijie Wang, Qiyu Kang, Rui She, Wei Wang, Kai Zhao, Yang Song, and Wee Peng Tay. HypLiLoc: Towards Effective LiDAR Pose Regression With Hyperbolic Fusion. In 2020 IEEE/CVF Conference on Computer Vision and Pattern Recognition, pp. 5176–5185, 2023.

Rukai Wei, Yu Liu, Jingkuan Song, Yanzhao Xie, and Ke Zhou. Exploring hierarchical information in hyperbolic space for self-supervised image hashing. IEEE Transactions on Image Processing, 2024.

Menglin Yang, Aosong Feng, Bo Xiong, Jihong Liu, Irwin King, and Rex Ying. Hyperbolic fine-tuning for large language models. arXiv preprint arXiv:2410.04010, 2024.

Zhewei Yao, Reza Yazdani Aminabadi, Minjia Zhang, Xiaoxia Wu, Conglong Li, and Yuxiong He. ZeroQuant: Efficient and Affordable Post-Training Quantization for Large-Scale Transformers. Advances in Neural Information Processing Systems, pp. 27168–27183, 2022.

Tao Yu and Christopher M De Sa. Numerically Accurate Hyperbolic Embeddings Using Tiling-Based Models. In Advances in Neural Information Processing Systems, volume 32, 2019.

Tao Yu, Toni J. B. Liu, Albert Tseng, and Christopher De Sa. Shadow Cones: A Generalized Framework for Partial Order Embeddings. In International Conference on Learning Representations, 2024.

Li Yuan, Tao Wang, Xiaopeng Zhang, Francis EH Tay, Zequn Jie, Wei Liu, and Jiashi Feng. Central Similarity Quantization for Efficient image and Video Retrieval. In 2020 IEEE/CVF Conference on Computer Vision and Pattern Recognition, pp. 3083–3092, 2020.

A Hyperbolic Machine Learning Preliminaries

Hyperbolic geometry is non-Euclidean geometry characterized by a constant negative curvature. Unlike Euclidean geometry, hyperbolic space exhibits unique properties, such as the exponential growth of volume (Ganea et al., 2018b) with respect to the radius and the divergence of parallel lines. It serves as a powerful mathematical framework for modeling hierarchical data, tree-like structures, and other settings where distances grow exponentially.

Hyperbolic spaces are equipped with several equivalent models Cannon et al. (1997) that offer different perspectives on the same underlying geometry. These models provide flexibility for computation, visualization, and mathematical reasoning. Despite their different formulations, they are isometric, meaning their distance metrics can be transformed into one another through well-defined coordinate transformations.

A.1 Five Common Models of Hyperbolic Geometry

Following the conventions in differential geometry, the five commonly used models of hyperbolic geometry are isometric to each other:

1. Halfspace Model (H): Also known as the Poincaré halfspace model, it is defined as:

$$H = \{(1, x_2, \ldots, x_{n+1}) : x_{n+1} > 0\}.$$

In this model, hyperbolic space is represented within a half-plane or half-space above a given axis, often used in complex analysis and conformal mapping.

2. Interior of the Disk Model (I): Also known as the Poincaré disk model, it is given by:

$$I = \left\{(x_1, \ldots, x_n, 0) : x_1^2 + \cdots + x_n^2 < 1\right\}.$$

Here, the hyperbolic space resides inside a Euclidean unit disk. This model is conformal, preserving angles, and is commonly used in visualization.

3. Jemisphere Model (J): Pronounced with the "J" as in Spanish, this model is defined as:

$$J = \left\{(x_1, \ldots, x_{n+1}) : x_1^2 + \cdots + x_{n+1}^2 = 1 \text{ and } x_{n+1} > 0\right\}.$$

The hyperbolic space is represented as a hemisphere of a unit sphere.

4. Klein Model (K): This model, known for its projective properties, is given by:

$$K = \left\{(x_1, \ldots, x_n, 1) : x_1^2 + \cdots + x_n^2 < 1\right\}.$$

The Klein model preserves straight-line geodesics, making it useful for certain computations, though it does not preserve angles.

5. Loid Model (L): Short for the hyperboloid model, it is defined as:

$$L = \left\{(x_1, \ldots, x_n, x_{n+1}) : x_1^2 + \cdots + x_n^2 - x_{n+1}^2 = -1 \text{ and } x_{n+1} > 0\right\}.$$

This model is particularly important in physics and mathematics due to its direct connection to Lorentzian geometry and relativity.

A.2 Isometry Between Models

The equivalence of these models is established through isometric coordinate transformations, as detailed in Section 7 of Cannon et al. (1997). These transformations ensure that distances and geodesics remain invariant when transitioning between models, making them interchangeable depending on the application.

Remark Under the isometry defined in Cannon et al. (1997), Section 7, five hyperbolic models yield equivalent retrieval results.

Proof. Although we do not binarize other hyperbolic models, they can still use our binarization via isometry defined in hyperbolic geometry Cannon et al. (1997), with a single coordinates transformation. In particular, we give one example of how the Lorentz model $\mathcal{L}$ transforms to Poincaré disk model Radford et al. (2021) in one line:

$$\mathcal{L} \mapsto \mathbb{D} : (x_0, x_1, ..., x_n) \mapsto (\frac{x_1}{1 + x_0}, \frac{x_2}{1 + x_0}, ..., \frac{x_n}{1 + x_0}) \tag{12}$$

We similarly illustrate the other isometries following the convention in (Cannon et al., 1997):

From Lorentz model to Klein model:

$$(x_0, x_1, \cdots, x_n) \mapsto (x_1/x_0, x_2/x_0, \cdots, x_n/x_0). \tag{13}$$

From Lorentz model to Hemisphere model:

$$(x_0, x_1, \cdots, x_n) \mapsto (x_0/x_n, x_1/x_n, \cdots, x_{n-1}/x_n, 1/x_n). \tag{14}$$

From Hemisphere model to Poincaé Halfspace model:

$$(x_0, x_1, \cdots, x_n) \mapsto (1, 2x_1/(x_0+1), \cdots, 2x_n/(x_0+1)) \tag{15}$$

From Hemisphere model to Poincaré Disk model:

$$(x_0, x_1, \cdots, x_n) \mapsto (x_0/(x_n+1), x_1/(x_n+1), \cdots, x_{n-1}/(x_n+1)) \tag{16}$$

Note that all the above transformations are isometry, meaning that the distance between source model embeddings is equal to the distance between the target model embeddings. Therefore, any hyperbolic model can benefit from our Poincaré binarization. □

A.3 Poincaré Ball Geometry

Hyperbolic geometry is a non-Euclidean geometry characterized by a constant negative curvature. Among the five commonly used models of hyperbolic geometry, we choose the Poincaré ball model due to its unique properties of isotropy and symmetry in each dimension. These properties make the Poincaré ball particularly well-suited for designing simple and effective binarization strategies.

The Poincaré ball model is defined as:

$$\mathbb{D}^n = \{\mathbf{x} \in \mathbb{R}^n : \|\mathbf{x}\| < 1\}, \tag{17}$$

where $\|\cdot\|$ denotes the Euclidean norm. Within this model, the geometry is described by a conformal Riemannian metric that preserves angles, making it especially convenient for embedding hierarchical or tree-like data structures.

The Riemannian metric of the Poincaré ball is given by:

$$g_{\mathbf{x}} = \lambda_{\mathbf{x}}^2 g^E, \tag{18}$$

where g^E is the Euclidean metric and $\lambda_{\mathbf{x}} = \frac{2}{1-\|\mathbf{x}\|^2}$ is the conformal factor. This conformal property ensures that local distances and directions are geometrically meaningful, while the ball's bounded nature simplifies computations and facilitates compact embedding representations.

A.4 Distance on Poincaré ball

Hyperbolic space can have different constant negative curvatures, parameterized by c. For simplicity, we follow the conventions in Ganea et al. (2018a); Shimizu et al. (2021) that use $c > 0$ to represent negative curvature to simplify computation. The Poincaré ball model with curvature c is defined as:

$$\mathbb{D}_c^n = \{\mathbf{x} \in \mathbb{R}^n : \|\mathbf{x}\| < \frac{1}{\sqrt{c}}\}, \tag{19}$$

where $\|\cdot\|$ denotes the Euclidean norm. The hyperbolic distance between two points $\mathbf{x}, \mathbf{y} \in \mathbb{D}_c^n$ under curvature c is given by:

$$d_c(\mathbf{x}, \mathbf{y}) = \frac{2}{\sqrt{c}} \tanh^{-1}\left(\sqrt{c}\,\|\ominus_c \mathbf{x} \oplus_c \mathbf{y}\|\right). \tag{20}$$

where the Möbius addition $\oplus_c$ and subtraction $\ominus_c$ are defined as:

$$\mathbf{x} \oplus_c \mathbf{y} = \frac{\left(1 + 2c\langle \mathbf{x}, \mathbf{y}\rangle + c\|\mathbf{y}\|^2\right)\mathbf{x} + \left(1 - c\|\mathbf{x}\|^2\right)\mathbf{y}}{1 + 2c\langle \mathbf{x}, \mathbf{y}\rangle + c^2\|\mathbf{x}\|^2\|\mathbf{y}\|^2}, \tag{21}$$

$$\mathbf{x} \ominus_c \mathbf{y} = \mathbf{x} \oplus_c (-\mathbf{y}), \tag{22}$$

$$\ominus_c \mathbf{x} = \mathbf{0} \oplus_c (-\mathbf{x}), \tag{23}$$

When $c = -1$, this reduces to the standard Poincaré ball distance:

$$d_{\mathbb{D}}(\mathbf{x}, \mathbf{y}) = \operatorname{arcosh}\left(1 + 2\frac{\|\mathbf{x} - \mathbf{y}\|^2}{(1 - \|\mathbf{x}\|^2)(1 - \|\mathbf{y}\|^2)}\right). \tag{24}$$

Here, c allows for the scaling of the hyperbolic space, with smaller $|c|$ corresponding to a "flatter" space.

A.4.1 Recovering Euclidean Space as $c \to 0$

As the curvature c approaches 0 (i.e., $c \to 0$), the hyperbolic space becomes increasingly flat, and its geometry converges to Euclidean geometry. Specifically:

- The radius of the Poincaré ball, $\frac{1}{\sqrt{c}}$, tends to infinity.
- The hyperbolic distance formula simplifies to the Euclidean distance:

$$\lim_{c \to 0^-} d_{\mathbb{D}_c}(\mathbf{x}, \mathbf{y}) = \|\mathbf{x} - \mathbf{y}\|. \tag{25}$$

- This occurs also because the conformal factor $\lambda_{\mathbf{x}} = \frac{2}{1 - c\|\mathbf{x}\|^2}$ in the Riemannian metric approaches 1, and the distortion due to curvature vanishes.,..

A.5 Poincaré Distance Symmetry Under Curvature c

We show that $d_c(\mathbf{x}, \mathbf{y})$ is symmetric, despite the non-commutative nature of the Möbius addition $\oplus_c$. This symmetry arises from the fact that the Euclidean norm of the Möbius addition is commutative. Specifically, the norm of the Möbius addition is given by:

$$\|\mathbf{x} \oplus_c \mathbf{y}\| = \sqrt{\frac{\|\mathbf{x}\|^2 + 2\langle \mathbf{x}, \mathbf{y} \rangle + \|\mathbf{y}\|^2}{1 + 2c\langle \mathbf{x}, \mathbf{y} \rangle + c^2 \|\mathbf{x}\|^2 \|\mathbf{y}\|^2}}. \tag{26}$$

The key observation here is that while $\mathbf{x} \oplus_c \mathbf{y} \neq \mathbf{y} \oplus_c \mathbf{x}$ in general, the norm satisfies:

$$\|\mathbf{x} \oplus_c \mathbf{y}\| = \|\mathbf{y} \oplus_c \mathbf{x}\|, \tag{27}$$

due to the symmetric structure of the numerator and denominator in the norm formula.

As a result, the hyperbolic distance $d_c(\mathbf{x}, \mathbf{y})$ becomes symmetric:

$$d_c(\mathbf{x}, \mathbf{y}) = d_c(\mathbf{y}, \mathbf{x}). \tag{28}$$

This property is crucial for defining a proper distance metric in hyperbolic space under curvature c.

B Real-valued Hyperbolic Embeddings

Given a training set $\mathcal{D}_{\text{train}} = \{(x_i, y_i)\}_{i=1}^N$. For each class y, let $\boldsymbol{p}_y$ denote its prototype target in a hyperbolic embedding space. We aim to train a network $f(\cdot)$ that projects the data point x onto hyperbolic space $\mathbf{x} = f(x)$, where $f(\cdot)$ is an arbitrary backbone network with an exponential map on top to project the output embedding to hyperbolic space. The likelihood of sample (x, y) is given as:

$$p(x|y = y') = \frac{\exp\left(-\mathrm{d}_{\mathbb{D}}(f(x), \boldsymbol{p}_{y'})\right)}{\sum_{y''}^{|\mathcal{H}|} \exp\left(-\mathrm{d}_{\mathbb{D}}(f(x), \boldsymbol{p}_{y''})\right)}, \tag{29}$$

which is optimized through the negative log-likelihood loss akin to Long et al. (2020). For the prototype embeddings of the classes, our approach works both in the one-vs-rest setting and the setting where we are equipped with label hierarchy $\mathcal{H}$. In the one-vs-rest setting, we can simply define class prototypes as maximally separated prototypes akin to Kasarla et al. (2022). In the hierarchical setting, we can obtain class prototypes for example using Hyperbolic Entailment Cones Ganea et al. (2018b).

C Proofs

Proposition C.1. *Given query* $\mathbf{q}$*, For any* $\mathbf{x}_1, \mathbf{x}_2$ *in the database such that* $|\|\mathbf{x}_1\| - \|\mathbf{x}_2\|| = \epsilon$*, given the Poincar'e disk boundary tolerance margin* δ*, if* $0 \leq \epsilon \leq \delta \frac{\mathrm{d}_{\mathbb{R}}(\mathbf{q}, \mathbf{x}_2) - \mathrm{d}_{\mathbb{R}}(\mathbf{q}, \mathbf{x}_1)}{\mathrm{d}_{\mathbb{R}}(\mathbf{q}, \mathbf{x}_2)}$*, then* $\mathrm{d}_{\mathbb{R}}(\mathbf{q}, \mathbf{x}_1) \leq \mathrm{d}_{\mathbb{R}}(\mathbf{q}, \mathbf{x}_2)$ *implies* $\mathrm{d}_{\mathbb{D}}(\mathbf{q}, \mathbf{x}_1) \leq \mathrm{d}_{\mathbb{D}}(\mathbf{q}, \mathbf{x}_2)$.

Proof. we start the analysis from the fact that poincar'e disk usually defines a tolerance margin δ such that

$$||x||^2 \leq 1 - \delta \tag{30}$$

to avoid numerical instability. For example, Khrulkov et al. (2020) adopted $\delta = 10^{-3}$ as the margin.

we show that 1) preserving $\mathrm{d}_{\mathbb{D}}(q, x_1) < \mathrm{d}_{\mathbb{D}}(q, x_2)$ is equivalent to $r \in (L, R)$ for some L, R.

Note that $\mathrm{d}_{\mathbb{D}}(q, x_1) < \mathrm{d}_{\mathbb{D}}(q, x_2)$ is equivalent to

$$\cosh^{-1}\left(1 + 2\frac{||q - x_1||^2}{(1 - ||q||^2)(1 - ||x_1||^2)}\right) < \cosh^{-1}\left(1 + 2\frac{||q - x_2||^2}{(1 - ||q||^2)(1 - ||x_2||^2)}\right). \tag{31}$$

As $\cosh^{-1}(\cdot)$ is strictly increasing, $\mathrm{d}_{\mathbb{D}}(q, x_1) < \mathrm{d}_{\mathbb{D}}(q, x_2)$ is equivalent to

$$\frac{||q - x_1||^2}{(1 - ||q||^2)(1 - ||x_1||^2)} < \frac{||q - x_2||^2}{(1 - ||q||^2)(1 - ||x_2||^2)}, \tag{32}$$

which is equivalent to

$$(||q - x_1||^2)(1 - ||x_2||^2) < (||q - x_2||^2)(1 - ||x_1||^2). \tag{33}$$

With simplified notation as:

$$\mathrm{d}_{\mathbb{R}}(q, x_1)^2(1 - r^2) < \mathrm{d}_{\mathbb{R}}(q, x_2)^2(1 - (r \pm \epsilon)^2). \tag{34}$$

Solving this quadratic inequality with respect to r, we have $r \in (L, R)$, where

$$L = \frac{\pm\epsilon \mathrm{d}_{\mathbb{R}}(q, x_2) - \sqrt{(\mathrm{d}_{\mathbb{R}}(q, x_2) - \mathrm{d}_{\mathbb{R}}(q, x_1))^2 + \epsilon^2(2\mathrm{d}_{\mathbb{R}}(q, x_2)^2 - \mathrm{d}_{\mathbb{R}}(q, x_1))}}{\mathrm{d}_{\mathbb{R}}(q, x_2) - \mathrm{d}_{\mathbb{R}}(q, x_1)}, \tag{35}$$

$$R = \frac{\pm\epsilon \mathrm{d}_{\mathbb{R}}(q, x_2) + \sqrt{(\mathrm{d}_{\mathbb{R}}(q, x_2) - \mathrm{d}_{\mathbb{R}}(q, x_1))^2 + \epsilon^2(2\mathrm{d}_{\mathbb{R}}(q, x_2)^2 - \mathrm{d}_{\mathbb{R}}(q, x_1))}}{\mathrm{d}_{\mathbb{R}}(q, x_2) - \mathrm{d}_{\mathbb{R}}(q, x_1)}, \tag{36}$$

leading to the following inequalities:

$$L < \frac{\pm\epsilon \mathrm{d}_{\mathbb{R}}(q, x_2) - \sqrt{(\mathrm{d}_{\mathbb{R}}(q, x_2) - \mathrm{d}_{\mathbb{R}}(q, x_1))^2}}{\mathrm{d}_{\mathbb{R}}(q, x_2) - \mathrm{d}_{\mathbb{R}}(q, x_1)} \tag{37}$$

$$\leq \frac{\epsilon \mathrm{d}_{\mathbb{R}}(q, x_2) - \sqrt{(\mathrm{d}_{\mathbb{R}}(q, x_2) - \mathrm{d}_{\mathbb{R}}(q, x_1))^2}}{\mathrm{d}_{\mathbb{R}}(q, x_2) - \mathrm{d}_{\mathbb{R}}(q, x_1)} = \epsilon\frac{\mathrm{d}_{\mathbb{R}}(q, x_2)}{\mathrm{d}_{\mathbb{R}}(q, x_2) - \mathrm{d}_{\mathbb{R}}(q, x_1)} - 1 \tag{38}$$

$$R > \frac{\pm\epsilon \mathrm{d}_{\mathbb{R}}(q, x_2) + \sqrt{(\mathrm{d}_{\mathbb{R}}(q, x_2) - \mathrm{d}_{\mathbb{R}}(q, x_1))^2}}{\mathrm{d}_{\mathbb{R}}(q, x_2) - \mathrm{d}_{\mathbb{R}}(q, x_1)} \tag{39}$$

$$\geq \frac{-\epsilon \mathrm{d}_{\mathbb{R}}(q, x_2) + \sqrt{(\mathrm{d}_{\mathbb{R}}(q, x_2) - \mathrm{d}_{\mathbb{R}}(q, x_1))^2}}{\mathrm{d}_{\mathbb{R}}(q, x_2) - \mathrm{d}_{\mathbb{R}}(q, x_1)} = -\epsilon\frac{\mathrm{d}_{\mathbb{R}}(q, x_2)}{\mathrm{d}_{\mathbb{R}}(q, x_2) - \mathrm{d}_{\mathbb{R}}(q, x_1)} + 1, \tag{40}$$

which means the quadratic inequality $\mathrm{d}_{\mathbb{R}}(q, x_1)^2(1 - r^2) < \mathrm{d}_{\mathbb{R}}(q, x_2)^2(1 - (r \pm \epsilon)^2)$ holds true when

$$\epsilon\frac{\mathrm{d}_{\mathbb{R}}(q, x_2)}{\mathrm{d}_{\mathbb{R}}(q, x_2) - \mathrm{d}_{\mathbb{R}}(q, x_1)} - 1 \leq -1 + \delta \tag{41}$$

$$-\epsilon\frac{\mathrm{d}_{\mathbb{R}}(q, x_2)}{\mathrm{d}_{\mathbb{R}}(q, x_2) - \mathrm{d}_{\mathbb{R}}(q, x_1)} + 1 \leq 1 - \delta \tag{42}$$

holds, leading that

$$\epsilon \leq \delta\frac{\mathrm{d}_{\mathbb{R}}(q, x_2) - \mathrm{d}_{\mathbb{R}}(q, x_1)}{\mathrm{d}_{\mathbb{R}}(q, x_2)}$$

Therefore, we conclude that the upper bound of ϵ is $\epsilon \leq \delta\frac{\mathrm{d}_{\mathbb{R}}(q,x_2)-\mathrm{d}_{\mathbb{R}}(q,x_1)}{\mathrm{d}_{\mathbb{R}}(q,x_2)} = \frac{\mathrm{d}_{\mathbb{R}}(q,x_2)-\mathrm{d}_{\mathbb{R}}(q,x_1)}{\mathrm{d}_{\mathbb{R}}(q,x_2)}$. We also have a trivial lower bound of ϵ, as $\epsilon \geq 0$, this is because when $\epsilon = 0$, we easily have $L = -1, R = 1$, are the boundary of the Poincare disk, leading to a **constantly true proposition**. □

Proposition C.2. *(Binary Ranking Preservation) For a binarizer $g(\cdot)$ such that $\langle \mathbf{x}^+, \mathbf{y}^+ \rangle \propto \langle g(\mathbf{x}), g(\mathbf{y}) \rangle$, $\mathrm{d}_{\mathbb{D}}(\mathbf{x}, \mathbf{y})$ is yields the same ranking results to Hamming distance $\mathrm{d}_{\mathbb{H}}(\mathbf{x}^b, \mathbf{y}^b) = \|\mathbf{x}^b \oplus \mathbf{y}^b\|_0$ for nearest neighbor search.*

Proof. For any binary representation $\mathbf{x}^b = g(\mathbf{x}), \mathbf{y}^b = g(\mathbf{y})$, the squared Euclidean distance $\mathrm{d}_{\mathbb{R}}$ is proportional to Hamming distance $\mathrm{d}_{\mathbb{H}}$:

$$\begin{aligned} d^2_{\mathbb{R}}(\mathbf{x}, \mathbf{y}) = d^2_{\mathbb{R}}(\mathbf{x}^+, \mathbf{y}^+) &= \|\mathbf{x}^+ - \mathbf{y}^+\|^2 \\ &= \|\mathbf{x}^+\|^2 + \|\mathbf{y}^+\|^2 - 2\langle \mathbf{x}^+, \mathbf{y}^+ \rangle \\ &\propto \|g(\mathbf{x})\|^2 + \|g(\mathbf{y})\|^2 - 2\,\langle g(\mathbf{x}), g(\mathbf{y})\rangle \\ &= \|\mathbf{x}^b\|^2 + \|\mathbf{y}^b\|^2 - 2\langle \mathbf{x}^b, \mathbf{y}^b \rangle \\ &= \mathrm{d}_{\mathbb{H}}(\mathbf{x}^b, \mathbf{y}^b). \end{aligned} \tag{43}$$

Following Proposition C.2, we have nearest neighbor equivalence between the Hamming distance and hyperbolic distance:

$$\begin{aligned} \arg\min_{\mathbf{x}} \mathrm{d}_{\mathbb{H}}(\mathbf{q}, \mathbf{x}) &= \arg\min_{\mathbf{x}} d^2_{\mathbb{R}}(\mathbf{q}, \mathbf{x}) \quad \text{by equation 43} \\ &= \arg\min_{\mathbf{x}} \mathrm{d}_{\mathbb{R}}(\mathbf{q}, \mathbf{x}) \\ &= \arg\min_{\mathbf{x}} \mathrm{d}_{\mathbb{D}}(\mathbf{q}, \mathbf{x}) \quad \text{by Prop. C.1.} \end{aligned} \tag{44}$$

□

Corollary C.3. *Under the condition of Proposition C.2, hyperbolic metric $d_{\mathbb{D}}(\mathbf{x}, \mathbf{y})$ is ranking preserving as euclidean metric $\mathrm{d}_{\mathbb{R}}(\mathbf{x}, \mathbf{y})$.*

Proof. Given query $\mathbf{q}$ and database $\mathcal{X} = \{\mathbf{x}_i\}$, we annotate the subscript of the database according to the Euclidean distance to the query. such that:

$$\mathrm{d}_{\mathbb{R}}(\mathbf{q}, \mathbf{x}_1) \leq \mathrm{d}_{\mathbb{R}}(\mathbf{q}, \mathbf{x}_2) \leq \cdots \leq \mathrm{d}_{\mathbb{R}}(\mathbf{q}, \mathbf{x}_N) \tag{45}$$

From Proposition C.2, we can have:

$$\mathrm{d}_{\mathbb{D}}(\mathbf{q}, \mathbf{x}_1) \leq \mathrm{d}_{\mathbb{D}}(\mathbf{q}, \mathbf{x}_2) \leq \cdots \leq \mathrm{d}_{\mathbb{D}}(\mathbf{q}, \mathbf{x}_N) \tag{46}$$

□

This means under the conditions of Proposition C.2 the hyperbolic metric yields the same output ranking as using the Euclidean metric, leading to the same retrieval outputs.

D Slowness of Hyperbolic Space

The strongest evidence that hyperbolic space is more suitable for retrieval than Euclidean is its **compact nature**, as shown in (Long et al., 2020) and Ermolov et al. (2022). Unfortunately, this comes at the cost of **slowness** that is determined by the nature of the hyperbolic distance:

$$\mathrm{d}_{\mathbb{D}}(\mathbf{q}, \mathbf{x}) = \frac{2}{\sqrt{c}} \tanh^{-1}\left(\sqrt{c}\left\|\frac{\left(1 - 2c\langle \mathbf{q}, \mathbf{x}\rangle + c\|\mathbf{x}\|^2\right)\mathbf{q} + \left(1 - c\|\mathbf{q}\|^2\right)\mathbf{x}}{1 - 2c\langle \mathbf{q}, \mathbf{x}\rangle + c^2\|\mathbf{q}\|^2\|\mathbf{x}\|^2}\right\|^2\right). \tag{47}$$

However, The efficiency brought by low-dimensional embedding is offset by its slow computation, in hyperbolic space, distance calculation is much slower than its Euclidean counterpart

$$\mathrm{d}_{\mathbb{R}}(\mathbf{x}, \mathbf{y}) = \|\mathbf{x} - \mathbf{y}\|^2. \tag{48}$$

We can quantitatively show how slow hyperbolic distance calculation is, as hyperbolic distance calculation takes 20.2713 ± 0.1443 micro-seconds, while its Euclidean counterpart takes 4.7033 ± 0.0394 micro-seconds. This result comes from 512-dim float number vectors distance calculations, averaged over 10^4 calculations on a single CPU core, both $\mathrm{d}_{\mathbb{D}}$ and $\mathrm{d}_{\mathbb{R}}$ are based on implementation of (Becigneul & Ganea, 2019).

To make hyperbolic space practically useful for retrieval, we need to bypass the need for explicit distance calculations in hyperbolic space. We present the necessary theory and algorithms to do so in our Binary Hyperbolic Embeddings.

D.1 Analysis for Lorentz model

The distance metric under Lorentz model is induced by *Lorentzian scalar product*:

$$\langle \mathbf{x}, \mathbf{y} \rangle_{\mathcal{L}} = x_0 y_0 + \sum_{i=1}^{n} x_i y_i \tag{49}$$

The associated distance is defined as:

$$d_{\mathbb{L}}(\mathbf{x}, \mathbf{y}) = cosh^{-1}\left(-\langle \mathbf{x}, \mathbf{y} \rangle_{\mathcal{L}}\right) \tag{50}$$

Although this distance appears to be fast to compute, we still suffer from the complexity of its anisotropic and unlimited range. Using Poincaré disk as a proxy also does not work, because transforming from Poincaré disk $\mathbb{D}$ to Lorentz model $\mathcal{L}$ also incurs high computation costs:

$$\mathbb{D} \mapsto \mathcal{L} : (\mathbf{x}) \mapsto \frac{(1 + \|\mathbf{x}\|^2, x_1, x_2, \cdots, x_n)}{1 - \|\mathbf{x}\|^2} \tag{51}$$

E More experiments

E.1 Effect of dimensionality and number of bits

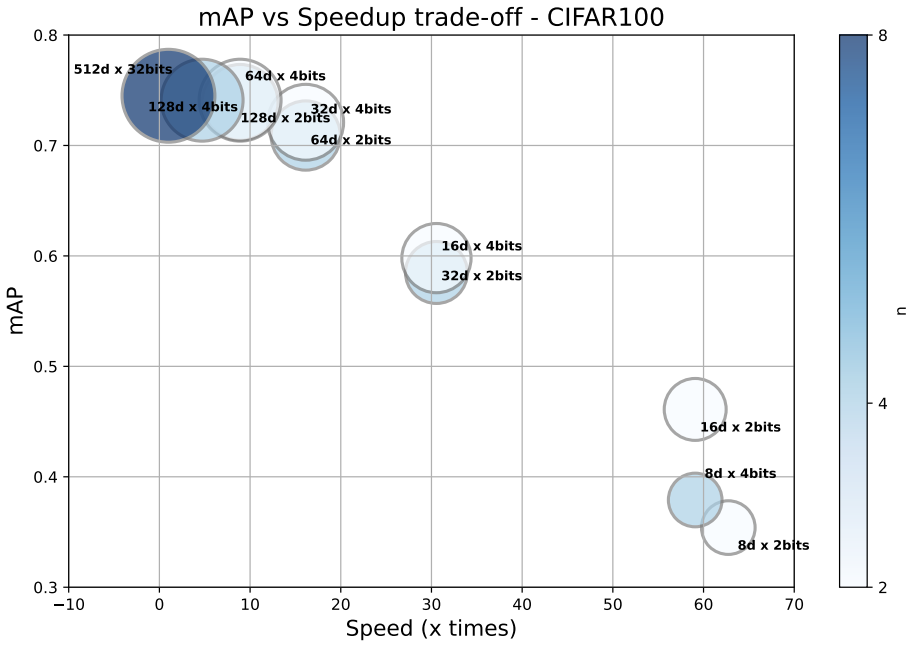

Figure 6: **The effect of embedding dimensions and quantization bits** on CIFAR100 on CLIP visual backbone. The darkest bubble denotes the full-precision Euclidean embedding. We find it is best to use more dimensions with strong compression than vice versa. With binary hyperbolic embeddings, we can obtain > 4.7 times faster retrieval speeds at roughly the same performance. Naturally, we can compress much further, at the cost of retrieval performance.

We visually show the speed-performance trade-off on CIFAR100 in Figure E.1. Lower bit/dimension configurations result in higher speeds (up to 62.73×) but lower mAP, while higher configurations provide better mAP (up to 0.745) at the cost of reduced speed (down to 4.71×). The best trade-off between speed and performance appears to be with binary hyperbolic embeddings, achieving over 8 times faster speeds with roughly the same performance. The highest mAP of 0.745 is achieved with both 128 × 2 = 256 and 128 × 4 = 512 configurations, with the latter offering slightly better speed. This underscores the balance between embedding dimensions, quantization bits, retrieval performance, and speed, highlighting the potential for significant speed-ups with only modest reductions in accuracy.

E.2 EFFECT OF HIERARCHICAL KNOWLEDGE

To measure this potential we follow Long et al. (2020); Ghadimi Atigh et al. (2021) in using the *Sibling mAP* (SmAP) performance metric. Building upon the mAP metric, SmAP takes into account the proximity in the class hierarchy for retrieved items. Specifically, when an item retrieved is just one hop away (i.e., same parent class) from the ground truth it is considered a true positive.

Table 8: **The effect of using hierarchical knowledge and different manifolds** on CIFAR100 on CLIP visual backbone. At full-precision, Spherical and hyperbolic embeddings outperform Euclidean embeddings, at the cost of a large number of bits and/or slow distance calculations. By binarizing we can maintain the performance benefits of hierarchy and hyperbolic embeddings but at a highly compressed bit length.
$\star$ denotes that the method has been modified to be using hyperbolic distance metric.

	Hierarchical	Manifold	Bit length	Binary	mAP	SmAP
Radford et al. Radford et al. (2021)	✗	$\mathbb{R}$	16,384	✗	0.721	0.835
Kasarla et al. Kasarla et al. (2022)	✗	$\mathbb{S}$	3,168	✗	**0.746**	0.860
Kasarla et al. Kasarla et al. (2022)$\star$	✗	$\mathbb{D}$	3,168	✗	0.744	0.863
Barz & Denzler Barz & Denzler (2020)	✓	$\mathbb{S}$	3,200	✗	0.719	0.843
Long et al. Long et al. (2020)	✓	$\mathbb{D}$	1,600	✗	**0.746**	**0.868**
Binary (ours)	✓	$\mathbb{D}$	512	✓	0.745	0.866

In Table 8 and 9 we perform a comparison to gain insight into the effect of using hierarchy and hyperbolic embeddings. We show that prior full-precision approaches perform comparable in terms of mAP when using a hyperbolic or Spherical manifold, and that adding hierarchy is especially beneficial to the SmAP performance. However, despite being more compressed than full-precision Euclidean manifolds these approaches still require a large number of bits and/or slow hyperbolic distance calculations. By binarizing, we are able to compress hierarchical hyperbolic embeddings to a small bit length whilst maintaining good performance on both standard and hierarchical metrics.

Table 9: **The effect of using hierarchical knowledge and different manifolds** on ImageNet1K on CLIP visual backbone. At full-precision Spherical and hyperbolic embeddings outperform Euclidean embeddings, at the cost of a large number of bits and/or slow distance calculations. By binarizing we can maintain the performance benefits of hierarchy and hyperbolic embeddings but at a highly compressed bit length.
$\star$ denotes that the method has been modified to be using hyperbolic distance metric.

	Hierarchical	Manifold	Bit length	Binary	mAP	SmAP
Radford et al. Radford et al. (2021)	✗	$\mathbb{R}$	16,384	✗	0.593	0.787
Kasarla et al. Kasarla et al. (2022)	✗	$\mathbb{S}$	3,168	✗	0.607	0.802
Kasarla et al. Kasarla et al. (2022)$\star$	✗	$\mathbb{D}$	3,168	✗	0.607	0.807
Barz & Denzler Barz & Denzler (2020)	✓	$\mathbb{S}$	3,200	✗	0.599	0.811
Long et al. Long et al. (2020)	✓	$\mathbb{D}$	1,600	✗	**0.610**	**0.815**
Binary (ours)	✓	$\mathbb{D}$	512	✓	0.608	0.812

E.3 EFFECT OF CURVATURE AND RADIUS

In Table 10, we explore the effect of curvature on the ImageNet1K dataset. The parameter r^2 represents the squared radius used for constructing class prototypes on the Poincaré disk, while c denotes the curvature used when optimizing the function to map data samples to class prototypes. Low curvature values indicate almost flat, Euclidean-like space, whereas high curvature values can cause numerical instability. Therefore, a medium curvature value is preferred for both class prototype embedding and sample embedding.

The table lists the accuracy results for different combinations of r^2 and c. For $r^2 = 10^3$, the accuracy improves from 0.493 with $c = 10^{-3}$ to 0.521 with $r^2 = 10^2$ and further to 0.587 with $r^2 = 10$. The best performance, with an accuracy of 0.608, is achieved with $r^2 = 1$ and $c = 10^{-2}$. As r^2

Table 10: **The effect of curvature** on ImageNet1K on CLIP visual backbone. Parameter r^2 is the squared radius used when constructing the class prototypes $\boldsymbol{P}$ on poincaré disk, whereas c is the curvature used when optimizing $f(\cdot)$ to map data samples to class prototypes. Low curvature indicates almost uncurved, euclidean-like space, whereas high curvature causes numerical instability. Thus, a medium value of curvature during both class prototype embedding and sample embedding will be preferred.

	$r^2 = 10^3$	$r^2 = 10^2$	$r^2 = 10$	$r^2 = 1$	$r^2 = 0.1$
$c = 10^{-3}$	0.493	0.521	0.587	0.596	0.588
$c = 10^{-2}$	-	0.586	0.599	**0.608**	0.594
$c = 0.1$	-	-	0.601	0.607	0.605
$c = 1$	-	-	-	0.549	0.550
$c = 10$	-	-	-	-	0.372

decreases further to 0.1, the accuracy decreases slightly. High curvature values ($c = 1$ and $c = 10$) result in significantly lower accuracy, highlighting the numerical instability.

In summary, medium curvature values during both class prototype embedding and sample embedding yield better performance, while high curvature causes numerical instability and lower accuracy.

F More Related Work

Hyperbolic representation differs from the Euclidean representation commonly used in deep learning. Early success was obtained by embedding the nodes of hierarchies as hyperbolic vectors, outperforming Euclidean embeddings. Nickel & Kiela (2017) introduce Poincaré Embeddings, where hierarchical nodes are positioned by pulling and pushing nodes based on parent-child relations. Ganea et al. (2018b) extend this idea through hyperbolic entailment cones, where child nodes should strictly fall under the cone spanned by parent nodes. Other hyperbolic embeddings Sala et al. (2018); Balazevic et al. (2019); Tseng et al. (2023); Yu et al. (2024) further explore these ideas for incomplete information, graphs, and generalibility, respectively. To make the step towards deep learning in hyperbolic space, Ganea et al. (2018a) and Shimizu et al. (2021) introduce hyperbolic linear, recurrent, convolutional, and self-attention layers in the most commonly used model of hyperbolic space: the Poincaré ball model. These works have served as a foundation for hyperbolic deep learning on graphs Pan & Wang (2021), dimensionality reduction Chami et al. (2021), complex networks Muscoloni et al. (2017), social media Sawhney et al. (2021), etc. For more details on hyperbolic layers, we refer to the survey of Peng et al. (2021).

Hyperbolic learning has also been broadly investigated in the image and video domain Mettes et al. (2023). Hyperbolic geometry has been shown to aid in a variety of tasks, including image segmentation Atigh et al. (2022), object detection Lang et al. (2022), action recognition Long et al. (2020); Peng et al. (2020), image-text representation learning Desai et al. (2023), representing 3D point clouds Montanaro et al. (2022) and LiDAR pose regression Wang et al. (2023). These works have in common that they leverage hierarchical knowledge to maximize the benefits from the hyperbolic space, embedding related concepts closer together, thereby allowing for more compact and powerful representations.